Simulating light quantity and quality over plant organs using a ray-tracing method to investigate plant responses in growth chambers

Sabine Demotes-Mainard, Hervé Autret, Christophe Pradal, Julien Le Gall, Vincent Guérin, Nathalie Leduc, Didier Combes, Christophe Renaud, Michaël Chelle, Jessica Bertheloot

▶ To cite this version:

Sabine Demotes-Mainard, Hervé Autret, Christophe Pradal, Julien Le Gall, Vincent Guérin, et al.. Simulating light quantity and quality over plant organs using a ray-tracing method to investigate plant responses in growth chambers. Biosystems Engineering, 2025, 258, pp.104256. ⟨10.1016/j.biosystemseng.2025.104256⟩. ⟨hal-05212812⟩

HAL Id: hal-05212812
https://hal.science/hal-05212812v1

Submitted on 21 Aug 2025

Biosystems Engineering 258 (2025) 104256

Contents lists available at ScienceDirect

Biosystems Engineering

journal homepage: www.elsevier.com/locate/issn/15375110

Research Paper

Simulating light quantity and quality over plant organs using a ray-tracing method to investigate plant responses in growth chambers

Sabine Demotes-Mainard [a,*], Hervé Autret [a], Christophe Pradal [b,c], Julien Le Gall [a], Vincent Guérin [a], Nathalie Leduc [a], Didier Combes [d], Christophe Renaud [e], Michaël Chelle [f], Jessica Bertheloot [a,1]

[a] Univ Angers, Institut Agro, INRAE, IRHS, SFR QUASAV, F-49000 Angers, France
[b] CIRAD, UMR AGAP Institut, 34398 Montpellier, France
[c] INRIA & LIRMM, Univ. Montpellier, CNRS, 34090 Montpellier, France
[d] INRAE, UR P3F, F-86600 Lusignan, France
[e] LISIC, Université du Littoral Côte d'Opale, Calais, France
[f] ECOSYS, INRAE, Université Paris-Saclay, Palaiseau, France

ARTICLE INFO

Keywords:
Light model
Phylloclimate
Controlled environment
Light spectrum
Branching
Rose

ABSTRACT

Ray-tracing models enable the assessment of light quantity and quality intercepted by plant organs, supporting biological studies in growth chambers with varying light conditions. However, their validation within canopies and clear usage methods remain limited. This work establishes a reliable method for using these models. The method includes i) accounting for the intensity and spectrum of light sources in the calibration procedure; ii) a generic calibration strategy using a few well-placed light measurement points based on chamber geometry. It evaluates the method to simulate light phylloclimate at the organ scale across biologically relevant wavebands of contrasted widths and properties. Using the SEC2 light simulation framework, three virtual experiments were conducted in a growth chamber, with and without rose plants. Inputs included chamber geometry, material optical properties, lamp emissions, and digitised plant mock-ups. Simulations were compared with spectral measurements at various chamber positions and sensor orientations, both without plants and inside a canopy. Results showed high accuracy in replicating spatial light variability, with RMSE ranging 0.011 to 0.021 and 0.014–0.038 μmol m^{-2}s^{-1}nm^{-1} across different wavebands and sensor orientations, for vertical and horizontal transects, respectively. Applying this approach to a case study demonstrated its effectiveness in formulating new biological hypotheses regarding the role of local light in regulating bud outgrowth. This was achieved by highlighting differences in phylloclimate induced by variations in plant architecture. This work thus provides a comprehensive framework for facilitating the application of ray-tracing models in growth chamber studies.

1. Introduction

The light perceived by different plant organs, called the light phylloclimate, determines plant growth by controlling organ photosynthesis and morphogenesis (*e.g.* branching, organ expansion) (Chelle, 2005; Demotes-Mainard et al., 2016; Evers et al., 2007; Natale et al., 2023). Both the overall irradiance in photosynthetically active radiation (PAR) and certain specific wavelengths that constitute morphogenetically active radiation (MAR) and are perceived by photoreceptors, are involved. Within a plant population, the light phylloclimate varies with the height, shape, and orientation of the organs, as well as with the architecture of neighbouring plants that intercept, reflect and transmit light according to their optical properties. Growth chambers are frequently used to study how plants respond to their light environment and are increasingly utilised for production in plant factories. Assessing the light phylloclimate in these settings is essential for a better understanding of plant processes and for adapting new crop production systems accordingly.

However, it is difficult to effectively measure the light phylloclimate as it would require a large number of sensors placed on different plant organs that could also modify growth by blocking light and potentially

---

* Corresponding author.
E-mail address: sabine.demotes-mainard@inrae.fr (S. Demotes-Mainard).
[1] Jessica Bertheloot present address: LEPSE, Univ Montpellier, INRAE, Institut Agro, Montpellier, France.

https://doi.org/10.1016/j.biosystemseng.2025.104256
Received 9 December 2024; Received in revised form 25 July 2025; Accepted 3 August 2025

Nomenclature

BRDF	bidirectional reflectance distribution function
BRTF	bidirectional reflectance transmittance function
FBV	flower bud visible stage
MAR	morphogenetically active radiation
MTG	Multiscale Tree Graphs
PAR	photosynthetically active radiation
PCV	petal colour visible stage
PPFD	photosynthetic photon flux density
rBias	relative bias
RMSE	root-mean-square error
rr	relative rank, from the plant base
rRMSE	relative root-mean-square error
r2	square of the Pearson correlation coefficient
sd	standard deviation

distorting organs by their weight. Light models, mainly developed through computer graphics (Pharr, Wenzel, & Humphreys, 2016) can accurately represent the spectral emission from light sources and calculate light propagation in complex environments, while also taking into account the physical characteristics of the materials with which light interacts, including plant organs themselves (Kahlen & Stützel, 2011; Sarlikioti, de Visser, Buck-Sorlin, & Marcelis, 2011).

Light models were first developed to represent field growing conditions (*e.g.*, the nested radiosity model of Chelle and Andrieu (1998). They were then applied to greenhouses, initially without accounting for the interaction of light with the greenhouse structure, and no lamps were simulated (Sarlikioti, de Visser, Buck-Sorlin, & Marcelis, 2011; Wiechers, Kahlen, & Stützel, 2011). Growth chambers present a more complex environment for light simulations due to the lighting system (anisotropic, potentially comprising multiple light sources with varying characteristics in intensities, directionalities and spectral LED diversity), the chamber physical structure (geometry), and the diverse properties of its materials. Thus, in a growth chamber without plants, light can vary substantially according to position, both on a horizontal plane and vertically (Boonen et al., 2002; Chelle, Renaud, Delepoulle, & Combes, 2007; Chenu, Rey, Dauzat, Lydie, & Lecoeur, 2008). This complexity increases further when crops are present, as light fluxes are additionally affected by plant architecture. Plant architecture alters the quantity and quality of light perceived by different organs of the same plant or by the same organ across different plants. This occurs in a dynamic manner over time, due to plant growth and the associated changes in architecture, creating a feedback loop where environmental conditions affect plant architecture, which in turn modifies light distribution and impacts growth. The structure and lighting system in a greenhouse plays a similar role to that in the growth chamber, with the addition of sunlight, which also interacts with the structure of the greenhouse. Due to this complexity, simulations of light environments using ray-tracing models were specifically developed for and applied on greenhouses and growth chambers that explicitly represent the greenhouse or growth chamber structure and its interaction with light (Chelle et al., 2007; de Visser, Buck-Sorlin, & van der Heijden, 2014; Henke & Buck-Sorlin, 2017; Hitz, Henke, Graeff-Hönninger, & Munz, 2019; Kim, Kang, & Son, 2020; Saito, Ishigami, & Goto, 2020). These models are based on a widely used method in optics that involves casting multiple rays from the light source to the plants and using the Monte Carlo method to solve the equations. This approach is very general and makes few assumptions, unlike other methods (e.g., radiosity, turbid model) (Chelle and Andrieu, 2006). It is particularly well-suited to the complexity of light simulations in growth chambers, accounting for factors such as high spatio-directional variability of light and surface anisotropy. Additionally, it enables the retrieval of light information at the organ scale, which requires a surface-based approach.

Such models, coupled with virtual plants, have proven useful to design the growing plant scene (*i.e.* the growing environment and plants). For example, they allowed optimisation of light source placement, the optical properties of the growth chamber materials, the light distribution from lamps, or the plant density with regard to the uniformity of light distribution, crop photosynthesis, light use efficiency or energy consumption (de Visser et al., 2014; Delepoulle, Renaud, & Chelle, 2008; Hitz et al., 2018, 2019; Kim et al., 2020; Lee et al., 2023; Saito et al., 2020). Modelling light interception at the level of individual plant organs provides insight into biological questions, including the role of local light on organ morphology (Hitz, Graeff-Hönninger, & Munz, 2020), the effect of light quality on crop performance by disentangling photomorphogenesis and photosynthetic contributions (Dieleman, De Visser, Meinen, Grit, & Dueck, 2019; Kalaitzoglou et al., 2021), and the influence of crop management on light interception and photosynthesis (Buck-Sorlin et al., 2011).

Using ray tracing models to simulate light conditions in growth chambers or greenhouse experiments requires a series of steps to virtually reproduce the experimental scene from measurements. In these models, the path of a ray in the growth chamber or greenhouse and the probability of being absorbed, reflected, or transmitted depends on the geometry, the position, and the optical properties of the objects in the space, and on the positions and characteristics of the light sources. Thus, the first step is to reconstruct the growth chamber or greenhouse (walls, ceilings, light sources, etc.) virtually, including plants, also digitally reconstructed. The emission of the lamps is described by their spectrum and their irradiance distribution in space (*i.e.* the photometric solid), the latter being either obtained from manufacturer data or from calibration on measurements (Buck-Sorlin et al., 2011; Hitz et al., 2019). The optical properties of inert materials and plant tissues are either obtained by measurement, from the literature or from calibration (Buck-Sorlin et al., 2011; Hitz et al., 2019; Saito et al., 2020). Virtual plants are reconstructed from phenotyping or simulated with 3D plant models (Hitz et al., 2020; Kim et al., 2020). Once the virtual scene is reconstructed, the simulations are calibrated on measured light data in the absence of plants, using sensors placed at the same positions, orientations, and view angles in both the virtual and real facilities (Hitz et al., 2019; Kim et al., 2020; Saito et al., 2020).

Across studies, there is however variability in how calibration points are selected. For example, Hitz et al. (2019) used measurements at six different heights in the centre of the growth chamber for optical properties calibration, and a single measurement at roughly mid-height of the chamber to adjust photon flux density. A single point, positioned centrally, was also used by Kim et al. (2020), but at the bottom of the chamber, and 124 measurements were employed by Saito et al. (2020), corresponding to 62 positions and two light intensities. Although these choices likely affect the simulations, no method has so far been proposed to rationalise them according to the main sources of light variability as the chamber geometry, the diversity of its materials, and the arrangement of the lamps.

The accuracy of ray tracing models coupled with digital reconstructions has also not been sufficiently evaluated, whereas it is essential for interpretation of results when these models are used to study plant response. For empty growth chambers, different studies using different ray tracing models in virtual chamber reconstructions showed good accuracy in simulating the spatial and angular distribution of irradiance measured in PAR (Chelle et al., 2007; Kim et al., 2020; Saito et al., 2020) and in wavelength bands of 100 nm width (Hitz et al., 2019). But the accuracy of the simulations was rarely evaluated within a plant population in the growth facility. When such evaluation was made, the spatial and angular variability was little explored, and the accuracy of the estimations in different light wavebands was not evaluated (Buck-Sorlin et al., 2011; Hitz et al., 2018; Kim et al., 2020). In particular, narrow bandwidths (<100 nm) have not previously been considered in evaluation studies, despite the fact that distinct morphological, physiological and molecular responses can be triggered by small shifts in wavelengths ranges, such as from amber (595 nm) to red (650 nm) (Yavari et al., 2021).

The objective of this study is to show and evaluate how to use ray tracing-based models to accurately simulate light quantity and quality variability within a canopy in a growth chamber. As in existing light simulation studies, a preliminary step of 3D reconstruction of the chamber and plants, along with the assignment of optical properties to the different elements, was performed. This work proposes a calibration method including the following innovations: i) a consideration of the intensity and spectrum of light emission sources upon completion of the light simulations, and ii) a generic strategy for identifying a few well-positioned light measurement points. The accuracy of the simulations was evaluated using a rosebush canopy as a model, considering various positions within the canopy, distances to the lamps and walls of the growth chamber, and sensor orientations, to mimic the positioning of different organs. In addition, the evaluation was undertaken for four ranges of wavelengths of contrasted widths that are differently absorbed by the vegetation and important for plant photosynthesis and photomorphogenesis: blue (400–500 nm), red (655–665 nm), far red (725–735 nm), and PAR (400–700 nm). The potential of this method is illustrated by its application to branching control in rosebush, which is a major determinant of plant visual quality and a process that is closely regulated by light (Corot et al., 2017; Garbez et al., 2015; Wubs, Heuvelink, Marcelis, Buck-Sorlin, & Vos, 2014). While reduced light intensity generally leads to decreased branching, an unexpected response has also been reported: the stimulation of branching after a temporary period of reduced light (Demotes-Mainard, Huché-Thélier, et al., 2013). It is hypothesised that this contrasting behaviour may be linked to differences in light interception by the organs, resulting from architectural changes in the plant bearing the buds in response to early light exposure. To test this hypothesis, the light model was used. The results provide insights into the potential mechanisms underlying the observed stimulation of branching.

2. Materials and Methods

2.1. The lighting simulator description

SEC2 is a lighting simulator dedicated to growth chambers that allows to estimate light distribution based on the photon tracing approach (used in computer graphics) which consists of tracing photons from the emission source (the light source) to the absorption point after several bounces on the 3D models surfaces following a stochastic ‘Monte Carlo’ approach (Chelle et al., 2007). SEC2 considers as input the 3D geometry of the growth chamber, its lighting system, plants, and the optical properties of the materials (reflectance, transmittance and specularity) that are specific to the wavelength considered for simulation. From these inputs, simulations are made for a wavelength or a wavelength band with homogenous optical properties. SEC2 enables the inclusion of different types of virtual sensors into the scene: (i) sensors that mimic the interaction of physical sensors in their interaction with light, (ii) virtual sensors that do not interact with light (used to map simulated light), (iii) sensors corresponding to a part of a plant tissue. Thus, the number of photons intercepted by each sensor or part of a plant tissue, can be counted. In addition, SEC2 can also provide views of the simulated scene.

2.2. Growth chamber description and reconstruction

The lighting simulator was used in the context of a growth chamber (Fig. 1) available at INRAE, Angers (France) and provided by Froid et Mesures (Beaucouzé, France). Briefly, a walk-in plant compartment containing a culture table is separated from a lamp compartment by a

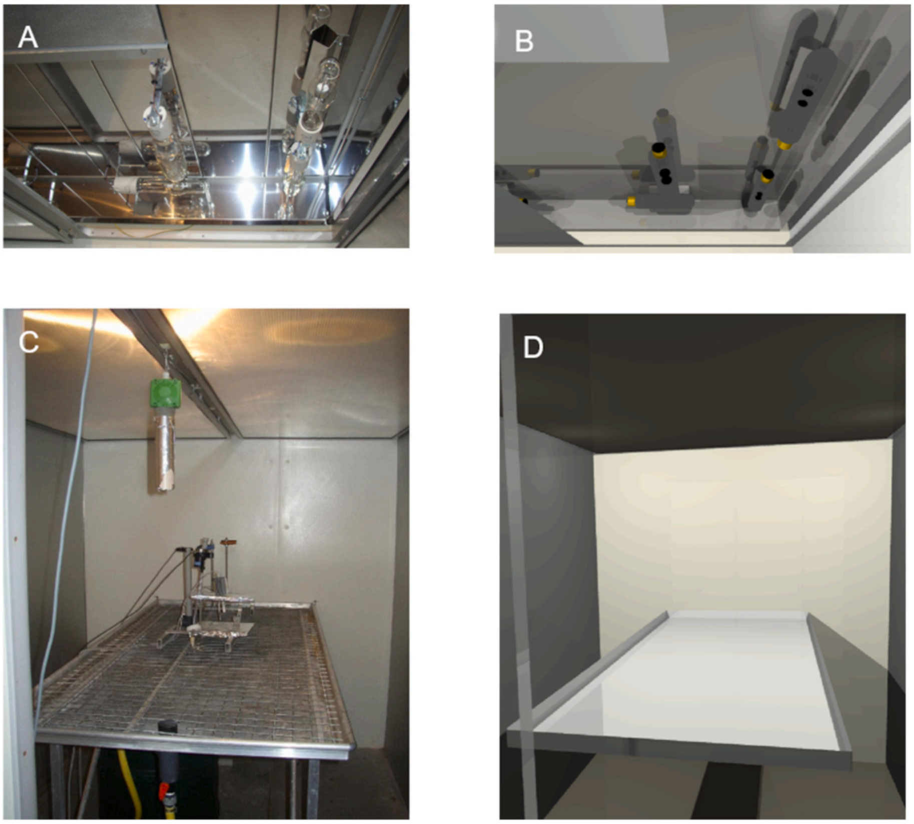

Fig. 1. Pictures and reconstruction of the growth chamber. Pictures of a quarter of the lamp compartment (A) and of the plant compartment (C), and the corresponding reconstructions (B, D).

translucent panel of cellular polycarbonate. The walls and table are composed of different materials detailed in Supplemental Material 1. Three metal halide lamps of 400 W and one of 1000 W (HQI, OSRAM, München, Germany) are positioned symmetrically in each of the four corners of the ceiling (16 lamps altogether). Each consists of a 20 mm-long light cylindric bulb having an opaque part at each end, absorbing the irradiance emitted along the direction of the bulb axis, and included in a larger bulb terminated on one side by a cap (Fig. 2A). The 400 W lamps are topped with a shiny metal baffle.

The walls of the plant and lamp compartments, the floor, the ceiling, the translucent panel separating the two compartments, the shiny metal baffles above the lamps, and the tabletop were all virtually reproduced. The translucent panel of polycarbonate separating the lamp compartment from the plant compartment, although cellular, was simplified as a unique homogeneous layer. Similarly, the material of the long walls, made of brushed metal and regularly perforated with small holes for ventilation, was represented as a homogeneous material, despite the presence of holes. The supports of the lamps, the door handle and the table legs were not reproduced, as it was assumed that due to their small size and position, they would not influence light distribution above the culture table. The virtual lamps must correctly reproduce the photometric solid of the real lamps, *i.e.* the irradiance distribution in the different directions around the lamp. It was quantified with a spectrophotometer Avantes (Avaspec-2048, Avantes, Eerbeek, Netherlands) by enclosing a lamp in a black box so as to suppress reflection by the surrounding materials. Assuming a symmetry of the photometric solid around the axis of the light bulb, the emitted irradiance was measured in a plane passing through the central axis of the bulb (Fig. 2A). Measurements were made each 15° on a half-circle of 50 cm radius centred on the light bulb central point. To virtually reproduce the measured photometric curve, the geometry of the real lamp was reproduced using a light source consisting in a filament of 20 mm-length, as cylindrical light sources do not exist in SEC2. At each end of the filament a black nonagon was placed to reproduce the opaque parts of the real lamp. The photometric curve was simulated using a device similar to the one used for measurements, with 10^8 photons emitted from the lamp with different sizes of nonagons. The best results were achieved with nonagons that fit inside a disk with a diameter of 24 mm. The measured photometric curve, and in particular the strong reduction of irradiance in the direction of the lamp axis, was correctly reproduced for each waveband of interest (§2.6.) (Fig. 2B).

2.3. Experiments

Three experiments were conducted. Exp. 1 and Exp. 2 aimed at evaluating the ability to simulate accurately the spatial variability in irradiance in two cases: (i) within the growth chamber in absence of plants (Exp. 1), when the anisotropic distribution of irradiance is generated by the growth chamber and its lighting system, and (ii) within a canopy in the growth chamber (Exp. 2), when plant architecture and optical properties contribute to the anisotropic distribution of irradiance. Whereas Exp. 3 aimed to illustrate how simulations can be used to give new insights in the regulation of a biological process using rose bush as plant species. Spectra measurements of incident irradiance were performed in the three experiments with a spectrophotometer measuring in the range 338–875 nm, with a spectral resolution smaller than 1 nm and equipped with a cosine corrector sensor to integrate the radiation on a half hemisphere. A first sensor was moved to various positions while a second sensor was fixed in place. Measurements from both sensors were synchronised, enabling corrections for any temporal fluctuations in light intensity.

In Exp. 1, only one group of four 400 W lamps were turned on (*i.e.* one 400W lamp in each quarter of the ceiling). Spectral measurements were taken by pointing the sensor upwards (elevation angle 90°) in a quarter of the chamber, acknowledging that the chamber is not strictly symmetrical across the quarters, as all elements are symmetrical along two axes, except for the culture table, which is only symmetrical along one of those axes. The 360 measurement points were taken sequentially and distributed according to a 10 cm × 10 cm mesh on three horizontal planes, at 10 and 50 cm above the table (corresponding to the height of Exp. 2–3 plants base and top, respectively, Fig. 3A), and at 90 cm above the table (close to the lamps, 17 cm under the panel separating the lamp and plant compartments).

In Exp. 2, one group of four 400 W lamps were turned on and 16 rose

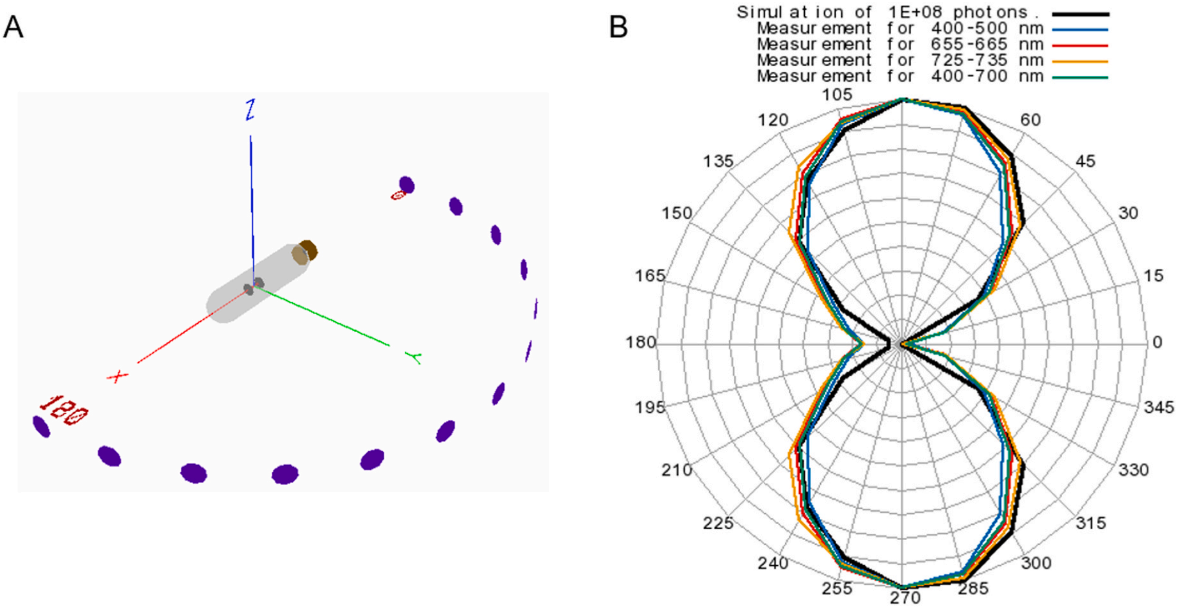

Fig. 2. Measured and simulated lamp photometric curves. (**A**) Sensor positions (blue dots) along a half-circle of 50 cm radius, centred on the light bulb central point for photometric curve measurement and simulation. The diagram depicts the real lamp, in the centre of which is positioned the light bulb. The two discs represent the black nonagons on each side of the filament of the virtual lamp. (**B**) Simulated (black line) and measured (coloured lines) normalised irradiance in blue, red, far-red, and PAR, with sensor positioned as in (A). The lamp bulb is oriented along the 0–180° axis. Measurements were completed by symmetry. (For interpretation of the references to colour in this figure legend, the reader is referred to the Web version of this article.)

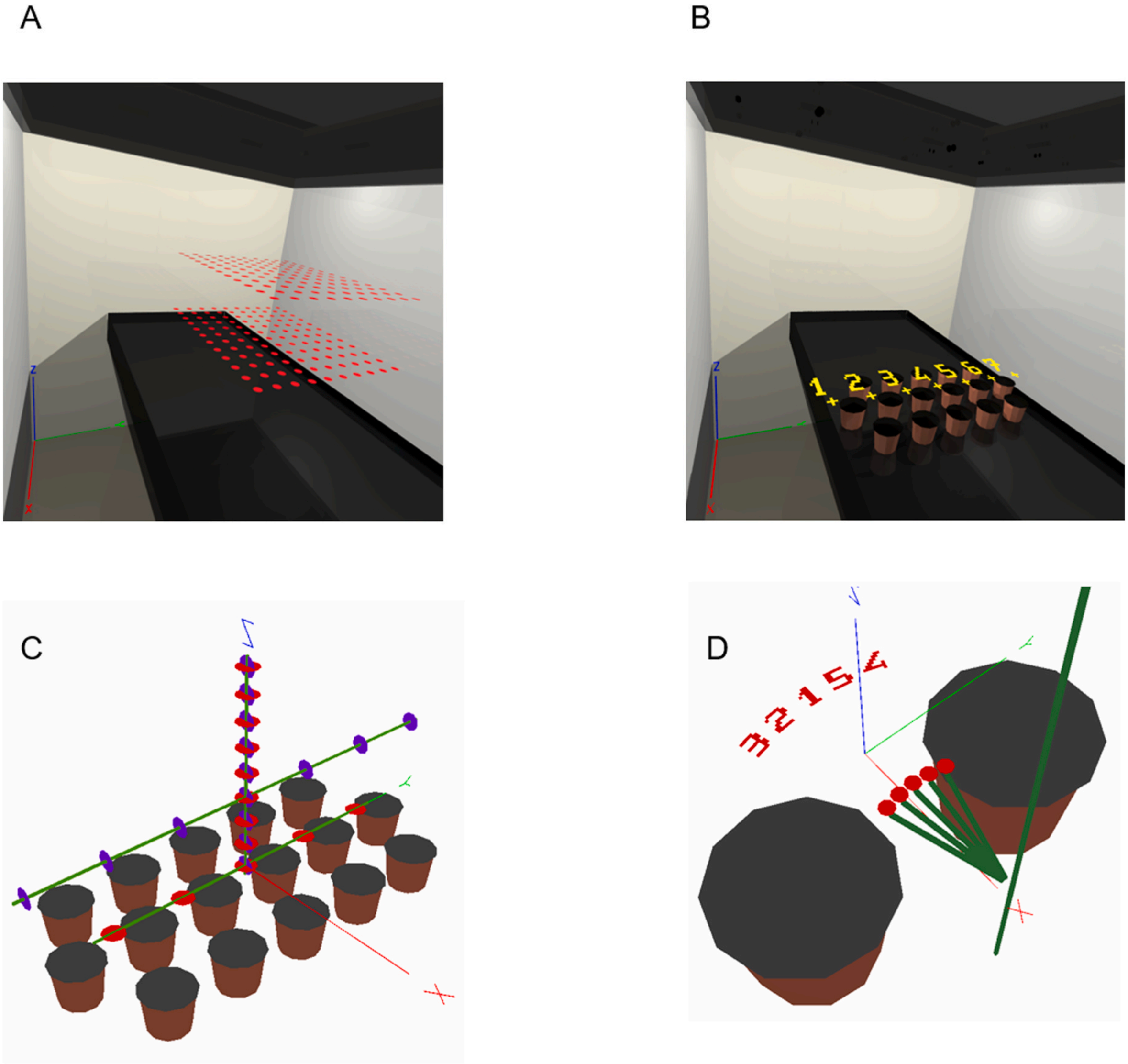

Fig. 3. Positions of the light sensor in Exp. 1 and Exp. 2. (**A**) In Exp. 1, the sensor was sequentially positioned to cover three planes in a quarter of the empty growth chamber, 10, 50 and 90 cm above the table (only 10 and 50 cm shown). (**B**) In Exp. 2, 16 plants were positioned in three staggered rows centred within the chamber, only the pots are represented here. Seven evenly spaced sites (yellow crosses) along the central row were defined. The sensor was positioned sequentially at the vertical of these sites. (**C**) In Exp. 2, the light sensor, pointing upward (red dots) or sideward (blue dots), was moved along a vertical transect centred in the chamber (at site 4). The sensor was also moved along two horizontal transects, one at 10 cm above the table, sensor pointing upward (red dots); and a transect at 25 cm above the table, sensor pointing sideward (blue dots). (**D**) For each position of the upward- and sideward-pointing sensor in (C), four complementary positions were utilised, each spaced 1 cm apart, represented by the red dots numbered 2, 3, 4 and 5. (For interpretation of the references to colour in this figure legend, the reader is referred to the Web version of this article.)

plants (*Rosa hybrida* 'Radrazz'), previously digitised (section 4), were positioned in three staggered rows, distant of 168 mm each, along the width of the culture table, with the central row positioned at the centre of the growth chamber (Fig. 3B). Each plant was in an 8 cm-high pot and was composed of a single stem (32.0 ± 2.7 cm long) bearing fully opened leaves and topped by a flower receptacle bearing sepals (the petals had fallen). Five different canopy configurations were successively created, in which the assignment of the 16 plants to each of the 16 positions and the plant azimuthal orientation were arranged randomly, creating different canopy architectures. The light sensor was positioned sequentially along horizontal and vertical transects, and oriented either upward (elevation angle 90°) or sideward (elevation angle 0°) to reproduce two extreme orientations of plant organs, typically horizontal mature leaflets and vertical stem segments (Fig. 3C). Seven sites (yellow crosses, Fig. 3B), evenly spaced, were defined along the central row, either half-way between two successive plants (sites 2 to 6), or beyond each border plant (sites 1 and 7). The sensor was positioned sequentially at the vertical of these sites for light measurements. For the vertical transect, the sensor was positioned at the midpoint of the canopy (site 4) and moved from the canopy base to the top each 5 cm from 10 to 50 cm above the table, with both upward and sideward orientation (Fig. 3C). For the horizontal transects, the sensor was positioned sequentially between two successive plants at the level of the central line of the plants (sites 2 to 6) or beyond each border plant (sites 1 and 7). For sensor pointing upward, the horizontal transect was placed at the canopy base, 10 cm above the table, moving the sensor from sites 2 to 6. For sensor pointing sideward, the horizontal transect was placed at the middle of the foliage at 25 cm above the table, vertically from sites 1 to 7 (Fig. 3B and C). The sideward pointing sensor faced the wall in front of site 7. The height of the horizontal trasects was chosen to maximise the quantity of plant tissue in the sensor field of view for each sensor orientation. At each position of the upward- and sideward-pointing sensor, four additional positions were used, two on either side of the central point, spaced 1 cm apart in an arc of circle. The sensor was rotated by 8° between each, attached to a 72 mm rotating stem (Fig. 3D). To capture the micro-local variability and represent the irradiance perceived at the scale of organs of approximately 4 cm long, the irradiance was averaged at the five measuring points. The mean values at each position were then averaged over the five canopy configurations, and standard deviation calculated to quantify the variability induced by changing plant architecture. In addition, in Exp. 2, the irradiance measurements were also taken at the same positions, with the same elevation angles (upward and sideward), when no plant was present on the table (configuration 0).

In Exp. 3, two groups of single-node cuttings of *R. hybrida* 'Radrazz' plants were obtained as described in Demotes-Mainard, Huché-Thélier, et al. (2013), at two successive periods. In each case, they were grown about four weeks in 500 ml pots containing a 50/40/10 mixture of neutral peat, coconut fibers and perlite in a temperature-controlled greenhouse and were kept disease-free, till a few days before bud outgrowth occurred on the cutting, at which they were transferred to the growth chamber (light/dark 16/8h photoperiod; 22/20 °C day/night temperature; air humidity 60–70 %) at a density of ca. 44 plants m^{-2}. Plants were sub-irrigated every two or three days with a fertilised solution. In the growth chamber the rose plants of the first group were grown under a constant high irradiance (HH modality; PPFD *ca.* 420 μmol m^{-2} s^{-1} at 30 cm above the culture table) until the petals of the flower bud became visible (petal colour visible stage; PCV), and the plants of the second group were grown under a low irradiance (PPFD *ca.* 100 μmol m^{-2} s^{-1} at 30 cm above the culture table) during the 16 days before the flower bud was visible on the primary axis (flower bud visible stage, FBV) followed by a high irradiance similar to HH modality (LH modality) until PCV stage. Given that FBV stage did not occur simultaneously, two identical chambers were used for LH modality, one with low irradiance, one with high irradiance, and each plant transferred from one to the other chamber at FBV stage. In this cultivar, bud outgrowth begins shortly after the FBV stage (Demotes-Mainard, Huché-Thélier, et al., 2013). From FBV, the development stage (dormant or outgrowing) of each axillary bud along the primary axis was scored every two or three days on 12 (HH) or 14 (LH) plants per modality. An axillary bud was considered to start its outgrowth when its first leaf was clearly visible between its scales. At FBV, plants consisted of a primary axis topped by the floral bud with *ca.* 8–9 foliated leaves and an axillary dormant bud at each leaf axil, the upper leaves and internodes were still rapidly expanding. About nine days later, at PCV stage, upper axillary buds had grown out into small new branches, the upper leaves and internodes were larger. At both stages, a subset of plants -including those monitored for bud outgrowth-were digitised as detailed below (section 2.4.). For the calibration of light simulations, irradiance was measured in the growth chamber without plants using a spectrophotometer, at 50 cm above the culture table (approximately canopy height) where irradiance was high. Measurements were taken at the four corners of the culture table, varying their distance from the two types of walls that make up the growth chamber (supplemental material 1 for wall description).

2.4. *Plant positioning, digitisation, and canopy reconstruction*

Canopies of Exp. 2–3 were described by each plant position on the culture table and each plant architecture obtained by digitisation (Polhemus 3Space Fastrack, Polhemus, Colchester, VT, USA, in Exp. 2; Immersion Microscribe G2L, Solution Technologies, Oella, MD, USA, in Exp. 3). The structure of a primary axis of a rose plant is described in Fig. S1A (Supplemental Material). The digitisation procedure, detailed in Supplemental Material 2, involved acquiring a sufficient number of 3D coordinates to reliably reconstruct the actual plant. Briefly, plant base, each leaf insertion point on the plant axes, and each leaflet insertion on the leaf rachis were recorded as well as leaflet orientation and size. In addition, the base and top of the floral organ were recorded. Diameters at the stem base and top were measured by a digital calliper. For Exp. 2, used for simulation validation, the plants were digitised at the end of their growth, once their architecture was fully developed, in order to avoid potential bias related to the time required for digitisation. For Exp. 3, a subset of plants constituting the canopy was digitised at FBV stage (34 and 24 plants for HH and LH, respectively) and at PCV stage (32, 24 plants for HH and LH; Fig. 4).

Digitisation information was converted into MTG format (Multiscale Tree Graphs) (Pradal et al., 2008, 2015) to reconstruct in 3D, with the OpenAlea PlantGL library (Pradal, Boudon, Nouguier, Chopard, & Godin, 2009), each of the 5 plant configurations of Exp. 2 (Fig. S1C, supplemental material 3) and each of the 2 canopies at two dates for Exp. 3 (Fig. 4B) (https://github.com/openalea/rose). Dataflows use a function that traverses MTGs, positions organs according to their 3D orientation, and builds 3D geometry of each organ (leaflets, internodes, flower buds). Details about the reconstructing procedure are given in supplemental material 3 and Fig. S1B (Supplemental Material). Plant 3D geometry obtained was visually checked by comparing it with the pictures taken on a subset of plants in Exp. 3 (an example of two plants at FBV and PCV stages in Fig. 4A). In Exp. 3, only a subset of 32–34 and 24 plants were digitised for HH and LH, respectively, due to time constraints. Consequently, a filling procedure was implemented. It involved randomly selecting and orienting (between -π +π) digitised plants and placing them on the culture table in place of the missing ones. Plant 3D reconstructions at their position and orientation in the growth chamber in each canopy, were converted into triangle sets for use as inputs of SEC2 light simulator.

2.5. *Measurements and calculation of optical properties for simulations*

Reflectance and transmittance spectra of all objects of the experimental scenes were measured from 325 to 1075 nm using a spectrometer ASD Fieldspec Dual (Malvern Panalytical, Malvern, United Kingdom) and an integrating sphere Licor 1800-12 (LICOR, Lincoln, Nebraska, USA). Measurements were taken at five randomly selected points for each material comprising the objects in the growth chamber, except for the perforated brushed metal of two of the walls and the textured metal of the soil (10 measurements), the translucent panel of cellular polycarbonate (16 measurements) and rose leaves (20 mature leaves in Exp. 2; 18 mature and young leaves in Exp. 3, leaf measurements were taken both on the abaxial and adaxial faces). To estimate the optical properties of the objects in the growth chamber for light simulations, the 400–800 nm range was divided in 12 bands (Fig. S2, Supplemental Material) that (i) allowed to reconstitute the PAR and the wavebands of physiological interest in the morphogenetically active radiation (MAR), as defined in (Escobar-Gutierrez et al., 2009): broadband blue (400–500 nm), narrowband blue (445–455 nm), green (500–600 nm), broadband red (600–700 nm), narrowband red (655–665 nm), broadband far-red (700–800 nm), and narrowband far-red (725–735 nm) and that (ii) showed fairly homogeneous values of quantitative incident, reflectance and transmittance spectra for all objects of the scene. This method of segmenting the spectrum is intended to ensure the same level of simulation accuracy in the PAR and each of the physiologically relevant bands in MAR.

A coefficient of reflectance and transmittance was then calculated for each of the 12 wavebands and materials, based on the average of the measured values. Young (leaflets not fully opened) and mature leaves (leaflets opened at 180°) were distinguished, and properties measured on the adaxial and abaxial side of the leaves were assigned to the triangles constituting each side. For the perforated brushed metal walls, it was previously confirmed (data not shown) that the mean reflectance was similar whether calculated (i) from randomly sampled points (data used here) or (ii) from points exclusively sampled within the metal area when the reflectance was weighted by the relative surface area of the metal and the holes in the wall, allowing a null reflectance for the surface of the holes. Specularity, which is the proportion of the reflected or

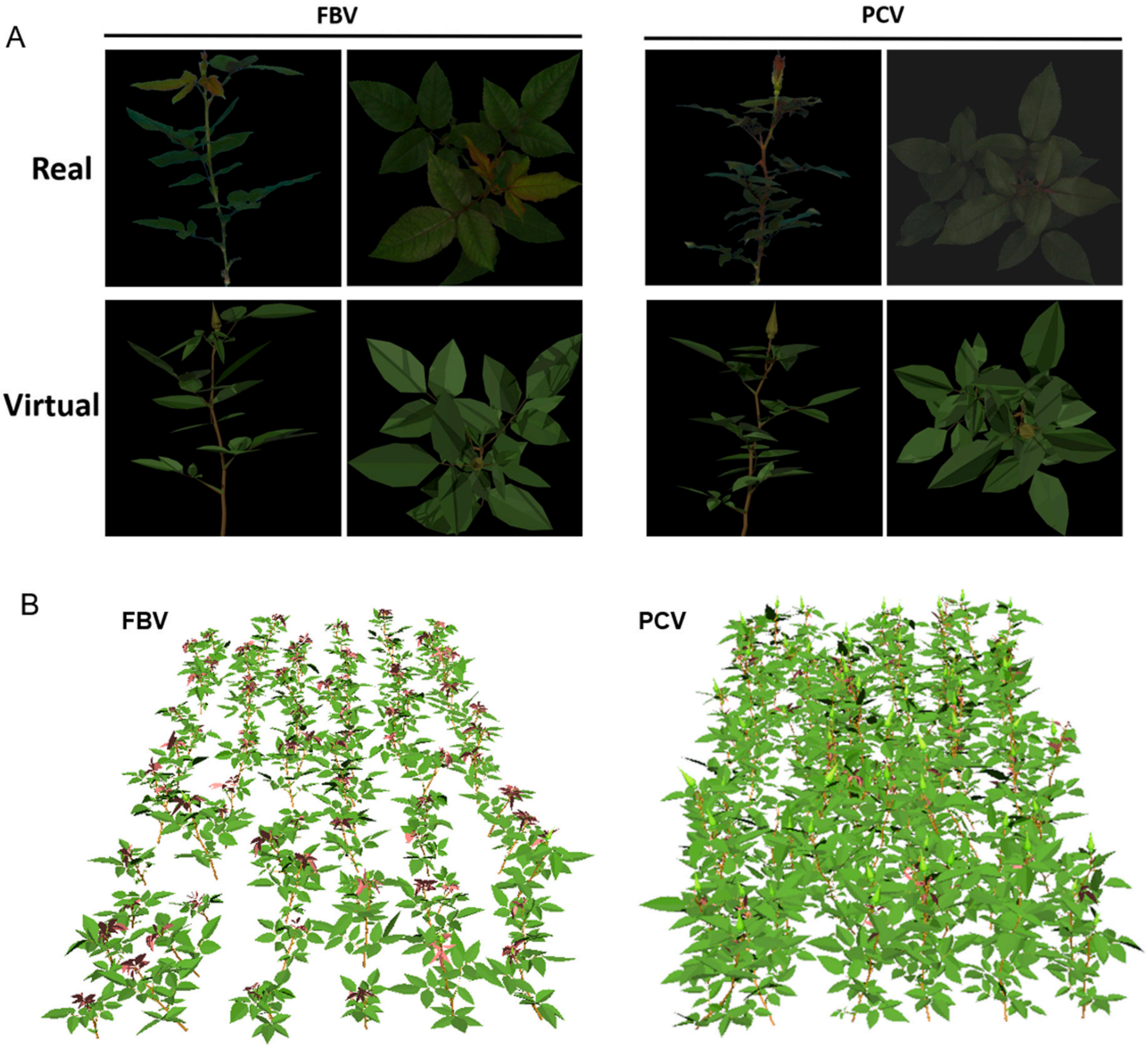

Fig. 4. Virtual reconstruction of rose plants. (A) Comparison between the architecture of a reconstructed rose primary axis and of the real one at stages FBV and PCV. For each stage, side and top views are represented. **(B)** Visualisation of reconstructed rose canopies, spreading all over the culture table (not represented) in the growth chamber, at stages FBV and PCV. Plants were those measured in Exp. 3, and for (B), under continuous high light intensity (HH modality).

transmitted radiation that goes in a preferred direction (*e.g.* for reflection, the inverse of the angle of incidence), could not be measured and was estimated from the visual aspect of each material with a unique value per material over the 400–800 nm range for reflected light (Supplemental Material 4); specularity was set to zero for transmitted light (rose leaves, translucent polycarbonate cellular panel).

2.6. *Light simulations*

Growth chamber and canopy reconstructions, as well as their optical properties, were set as input of SEC2 to simulate irradiance per wavelength band in the three experiments. Virtual sensors were positioned in the experimental scenes at the exact position and with the same elevation angle and field of view (180°) as physical sensors in Exp. 1 and 2. Sensor radius was 1 cm in Exp. 1, but in Exp. 2, where a more heterogeneous light distribution was expected due to the presence of plants, it was 0.25 cm to correspond to the size of the optical fibre sensor. In Exp. 3, the objective was to estimate light intercepted by the plant organs. For that, the different triangles composing the plant were considered as if they were sensors. For each experimental scene and each of the 12 wavebands of interest (Fig. S2, Supplemental Material), 10^{10} photons were launched, and 50 bounces were allowed for each photon; the simulations were repeated 10 times for Exp. 1 and Exp. 2 without plants. 10^{10} photons were sufficient as illustrated by a low coefficient of variation between the 10 repetitions for simulations in the empty growth chamber with sensors positioned and oriented as in Exp. 1 and 2 (Fig. S3, Supplemental Material).

These simulations account for differences between the wavebands of interest due to potential variations in the optical properties of the chamber materials across wavebands. However, they assume a homogeneous light spectrum, as 10^{10} photons are launched in each waveband. To account for light spectrum heterogeneity and the different sizes of the 12 wavebands of interest (Fig. S2, Supplemental Material), the simulated photon number received by each virtual sensor in a specific wavelength band (*e.g.*, 655–665 nm) was weighted by the ratio between the photon flux density emitted by the real lamp in that band and the lamp's total photon flux density in the range 400–800 nm. The simulation results are presented for four bands: blue (400–500 nm), red (655–665 nm), far red (725–735 nm), and the PAR (400–700 nm). These bands of physiological interest are differently absorbed by plant tissues. Since Blue and PAR are not among the 12 individually simulated wavebands but instead consist of three (400–445 nm, 445–455 nm, and 455–500 nm) and nine (400–445 nm, 445–455 nm, 455–500 nm, 500–534 nm, 534–542 nm, 542–600 nm, 600–655 nm, 655–665 nm, 655–700 nm) sub-bands, respectively, the simulation results for blue and PAR were obtained by summing the weighted simulated photon numbers of the three and nine bands, respectively.

The weighted simulated photon numbers were then converted into photon flux density (μmol photons m^{-2} s^{-1}) by calibration of irradiance measured on sensors in the real experiment in the growth chamber without plants. The calibration was made independently for each experiment (Exp.), to account for possible lamp aging or renewal, and for each wavelength band (λ). A subset of carefully selected points were chosen for measurements based on their location, ensuring they captured the range of observed light intensities and the effects of the materials constituting the growth chamber, as detailed in the Results section. Using these points, a linear relationship was established between the weighted simulated number of photons per unit area (N_{sim}) and measured μmol photons per unit area and time (N_{mes}), as follows:

For each Exp. and λ: $N_{mcs} = \alpha_0 + \alpha_1 \times N_{sim}$

where α_0 and α_1 are respectively the intercept and slope of the linear relationship.

The estimated coefficients α_0 and α_1 (Tab. S1 for estimated values, Supplemental Material) were then applied on the weighted simulated photon number at other locations in the growth chamber to obtain the irradiance distribution in the absence or presence of plants. When the calibrated simulated value was negative, it was set to 0.

2.7. Data analysis

Calculation and statistical analyses were made using R software (V 4.3.1, R Core Team, 2023). Linear relationships between N_{sim} and N_{mes} were estimated using lm(.) function. Biases for the intercept and slope were estimated using a non-parametric bootstrap approach using boot library (function *boot(.)*, 1000 bootstrap samples): they were calculated as the difference between the original parameters' estimate and the mean of the bootstrap parameters' estimate.

The agreement between irradiance simulations and measurements was assessed by the (i) root-mean-square error (RMSE) using hydroGOF package (Zambrano-Bigiarini, 2024), and relative RMSE (rRMSE) calculated as RMSE divided by the mean of measurements and expressed as a percentage, (ii) bias calculated as the mean of the differences between measurements and simulations, and relative bias (rBias) calculated as the bias divided by the mean of measurements, and (iii) r-square (r2) calculated as the square of the Pearson correlation coefficient (function cor(.)).

For light simulations on plant organs in Exp. 3, since all plant primary axes do not all have the same number of phytomers, plant organs were numbered according to their relative rank from the plant base (*rr*), as previously done for rose (Demotes-Mainard, Bertheloot, et al., 2013). The relative rank was calculated as:

$$rr = \frac{i - 1}{n - 1} \tag{1}$$

where *i* is the absolute rank of the foliated phytomer, counted from the base of the primary axis, and *n* the total number of foliated phytomers.

Relative rank 0 corresponds to the lowest leaf-bearing phytomer, 1 to the upper leaf-bearing phytomer.

Bud outgrowth rate was calculated as the proportion of buds that had grown out on the 12 and 14 plants for HH and LH, respectively. Individual leaf areas and internode lengths were quantified from digitised data. For each light modality of Exp. 3 (HH, LH), the patterns of bud outgrowth rate and irradiance distribution on leaves and internodes along rose axes were obtained by fitting observed data points by local polynomial regression (functions geom_smooth(method = 'lm') and geom_smooth(method = glm, method.args = list(family = "binomial"))).

3. Results

3.1. Selecting calibration points for accurate irradiance simulation in an empty growth chamber

A first step consisted in identifying how to convert the raw simulations of the light model, expressed in number of photons m^{-2}, into simulated irradiance expressed in μmol photons m^{-2} s^{-1}. This was made possible by correlating raw simulations and irradiance measurements in the empty growth chamber. Light simulations were performed and compared to measurements for a quarter of the growth chamber at 240 positions within two horizontal planes, one at 10 cm above the culture table (at plant base) and one at 50 cm (at plant top), with sensors pointing upwards (elevation angle = 90°) (Exp. 1; Fig. 3A). Since the model incorporates all physical interactions between light and the simulated growth chamber that lead to the complex spatial distribution of light within the growth chamber, the relationship should be linear. As expected, a linear model could be applied between simulations and measurements (assumption of normality and homoscedasticity satisfied, data not shown): the r^2 was high (Fig. 5; Table S1, Supplemental Material) and the estimated bias for the intercept and slope was low for all wavelength bands (Table S1, Supplemental Material). Small deviations were observed — specifically, a group of points located 50 cm above the table, and points with the lowest irradiance values at 10 cm above the table, which fell below the linear relationship shown in Fig. 5. Moreover, while there were no irradiance values near zero in the dataset, the estimated intercepts were not far but significantly different from zero (intercepts = 2.12, 0.42, 0.18, 9.6 μmol m^{-2} s^{-1}, for blue, red, far-red and PAR, respectively; $p\text{-value} < 0.0001$; Table S1, Supplemental Material). Thus, the light model and chamber reconstruction do not fully account for the real scene, and uncertainties in measurements, notably related to sensor position, can also contribute to discrepancies. However, given the overall high linearity between simulations and measurements, calibration of the simulations should be achievable using a linear relationship established from a limited number of measurement points, provided that they correspond to both low and high irradiance values. Using multiple points rather than a single one reduces the risk of obtaining a calibration that is overly specific to particular conditions.

To accurately estimate the linear relationship between model-simulated and observed values using a limited number of measurement points, it is essential to consider (i) both low and high irradiance values present in the chamber, which enables a precise estimation of the slope of this relationship, and (ii) the potential impact of the varying materials within the chamber, as they influence the paths of photons due to their optical properties. To define a protocol for selecting measurement points applicable to other growth chambers, the following guidelines are proposed (Table S2, Supplemental Material): choose positions (i) within the zone (volume) of interest (ii) where both high and low irradiance values are anticipated, based on the chamber's geometry, by varying the distance to the lamps (moving the sensor both horizontally and vertically), (iii) at varying distances from the different chamber's surfaces. Accordingly, 12 points were selected above the 1/4 culture table (avoiding walkways, rule i) for Exp. 1 calibration: one point at each corner of the 1/4 table at 10 and 50 cm above the table (eight points), thus varying the distance to the two different types of walls (rule iii) and from the lamps (rule ii), two points in its centre, away from the lamps, at 10 and 50 cm above the table, and two points that come closest to the vertical of the lamps at 50 cm above the table (rule ii). These points covered low, intermediate, and high irradiance values (Fig. S4, Supplemental Material).

These 12 measurement points were used to estimate the coefficients of the relationship between raw irradiance simulated by the light model and measured irradiance in each waveband of interest ($r^2 = 0.95$–0.96; Table S1, Supplemental Material). The coefficient values obtained using this small set of points were close to those obtained using the entire dataset (with confidence intervals overlapping those from the full

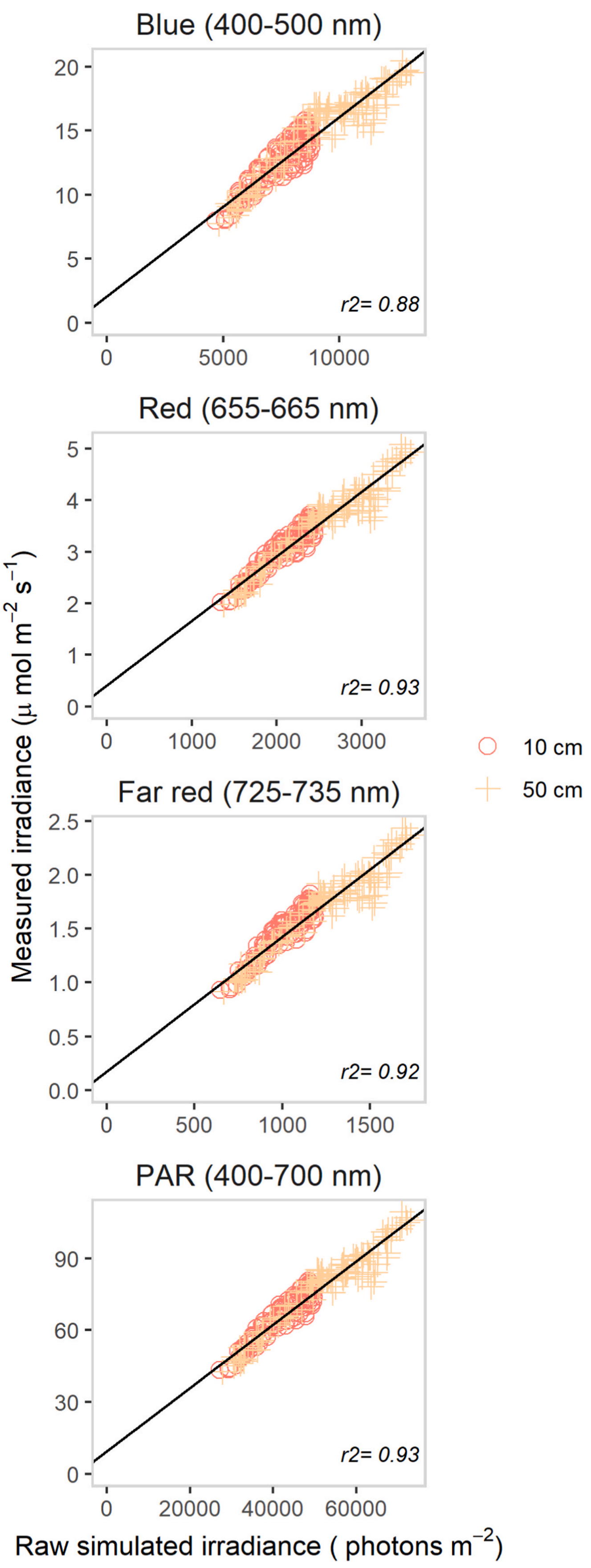

(caption on next column)

Fig. 5. Evaluation of the linearity between measured and raw simulated irradiance for different wavelengths of biological interest. The data come from Exp. 1 in the planes at 10 (red circles) and 50 cm (orange crosses) above the table. Raw simulated irradiances are calculated directly by SEC2, *i.e.* without any calibration procedure. The black line is the linear regression between measurements and simulations on all points. (For interpretation of the references to colour in this figure legend, the reader is referred to the Web version of this article.)

dataset, *i.e.* 240 points; Table S1). Applying this relationship on raw simulations at all other 228 locations to simulate irradiance, a good correlation was also obtained between irradiance simulations and measurements. The relative precision among the different wavelength bands studied was of the same order of magnitude, with relative root mean square errors ranging from 5.5 to 8.4 %, relative bias between −3.01 and 1.63 %, and r^2 between 0.88 and 0.93 (rRMSE, rBias and r^2 on Fig. 6). In detail, in the blue wavelength band, the rRMSE indicated a slightly lower accuracy than in the other wavebands, associated with over-estimation (rBias of −3.01 %). In addition, the irradiance spatial distribution was faithfully reproduced using data of Exp. 1 (Fig. 7). Irradiance was fairly stable at 10 cm above the table, while at 50 cm above the table, it increased to reach a maximum below the lamp, *i.e.* in the walkway ($Y > 137$ cm) at two-thirds of the distance between the back white wall and the middle of the chamber (X-axis) (Fig. 3A for chamber configuration). However, there was a discrepancy for a group of points located in the walkway at 50 cm ($Y > 137$ cm in Fig. 7; see also Fig. S5 (Supplemental Material) which is the equivalent to Fig. 6 but without the points in the walkway), for which irradiance was slightly overestimated in the four wavelength bands.

3.2. *Irradiance distribution trends within a rose canopy across varying canopy depth, distance to the walls, and plant architecture*

The accuracy of irradiance simulations was then tested regarding the irradiance variability in a rose canopy (Exp. 2; 16 previously-digitised plants staggered in three rows; Fig. 3C). Light sensors were moved along vertical (to grasp canopy depth effect) and horizontal (to grasp the distance to the walls effect) transects, and pointed either upward (elevation angle 90°) or sideward toward the wall in front of site 7 (Fig. 3B and C) (elevation angle 0°) to mimic what is perceived by leaves and stems, respectively. Five canopy configurations were created by changing plant positions to capture the variability caused by plant architectures around the sensors.

3.2.1. *Visualisations of the scene perceived by the sensors*

To facilitate the interpretation of the measurements and simulations, a visual representation of the scene as perceived by a sensor from different positions within the canopy is presented first (Fig. 8). Views correspond to the sensor in the central position (position 1 in Fig. 3D) with a 105° angle of view. The density of plant organs (stems and leaves) perceived by the sensor strongly increased when moving along the vertical transect from above the canopy to its base (Fig. 8A). Moreover, the changes were visually larger for a sensor pointing upward, than for a sensor pointing sideward, in line with the fact that the sideward-pointing sensor always perceives plant tissues even from above the canopy on the contrary to an upward-pointing sensor. When the sensor moved along the horizontal transect, the changes in the density of plant organs appeared visually smaller than for the vertical transect, especially with the sensor pointing upward (Fig. 8B). This illustrates a possible variability in irradiance linked to the position of an individual leaf in or outside the sensor field of view, for example, approximately half the field of view of the sensor pointing sideward at 35 cm perceived a single leaf close to the sensor.

3.2.2. *Calibration of the simulations in the empty growth chamber*

For calibration, eight points were identified where irradiance was

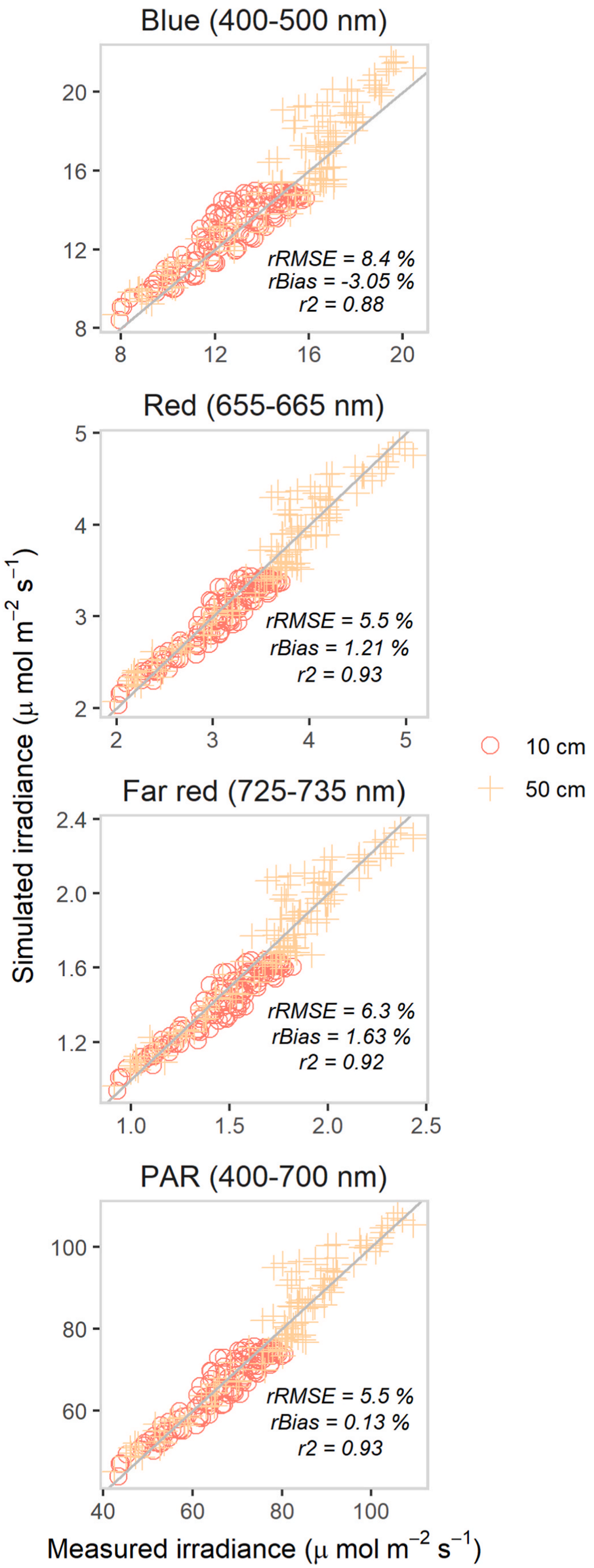

(caption on next column)

Fig. 6. Quality of model simulations in an empty growth chamber. Simulated *vs.* measured irradiance for different wavelengths of biological interest. The data come from Exp. 1 in the planes at 10 (red circles) and 50 cm (orange crosses) above the table. Simulations were obtained from model calibration on 12 chosen points. The line corresponds to y = x. (For interpretation of the references to colour in this figure legend, the reader is referred to the Web version of this article.)

measured in absence of plants based on the rule defined for Exp. 1: they were located at each end of transects, for the sensors oriented upward and sideward, to vary the height and the distance to the walls and lamps for each sensor orientation. These points covered the variability in irradiance registered by the light sensors (Fig. S6, Supplemental Material). The calibration line obtained with these eight points was also very close to that obtained with all the light measurement points in absence of plants, indicating that eight points well positioned were sufficient for the calibration.

3.2.3. Measured and simulated irradiance distributions within the canopy

The general trend of the simulated irradiance showed a high degree of agreement with the measurements in the different wavebands, both in terms of average irradiance over the five canopy configurations, and variability between the configurations (assessed by standard deviation) (Fig. 9). Irradiance was expressed per nm to facilitate comparison of spectral bands of different widths.

Along the vertical transect (Fig. 9A), simulations and measurements displayed, first, a greater mean attenuation for upward than for sideward sensors as expected from the above-described visualisations. Secondly, the measured and simulated variability of irradiance perceived by sensors pointing upward increased with canopy depth, reaching a maximum about halfway up the plants, before decreasing again at the canopy base. This pattern could be explained by leaf density pattern in the sensor field of view: in the upper canopy layers, there were only few and small plant surfaces intercepting light (floral receptacle, sepals, and small leaves with 1 or 3 leaflets, illustrated in Fig. 8A), and differences in plant architectures have little effect; moving downwards into the canopy, the leaves became more numerous and individual leaves larger, but still with light spots within the canopy, thus changes in the size and position of these leaves between configurations are likely to induce greater changes in nearby irradiance; in the bottom of the canopy, the number of leaves became large enough to create a radiative homogeneity. Thirdly, the simulated and measured variability of irradiance for sensors pointing sideward was more stable with canopy depth than for upward pointing sensors, in agreement with the observation that a sensor pointing sideward always had plant organs in its field of view, regardless of its position along the vertical profile (Fig. 8A). These results indicate that the variability induced by changes in plant architecture is not homogeneous along a vertical transect when perceived on a horizontal plane, as by horizontal leaves, but more homogeneous when perceived laterally, as by stem segments.

Along the horizontal transect (Fig. 9B), when sensors moved through the canopy away from a wall, the measured and simulated patterns of mean irradiance were, on the whole, flat. There was an exception for the sideward-pointing sensor positioned outside the canopy in front of the growth chamber wall (site 7), where the irradiance was slightly higher in the red and PAR wavebands, and to a lesser extent in the blue waveband, but not in the far-red. This observation is consistent with lower absorption of far-red light by leaves. The stability of irradiance along horizontal transects accounts for near-zero r^2 values observed for these transects, including in the far-red, where RMSEs are lowest. In contrast, high r^2 are observed for vertical transects. Moreover, the measured and simulated variability was also globally stable whatever the sensor orientation. The agreement between the simulated and observed standard deviations was good over the vertical transects, except for a systematic overestimation in the red and PAR wavelength bands with sideward-pointing sensors.

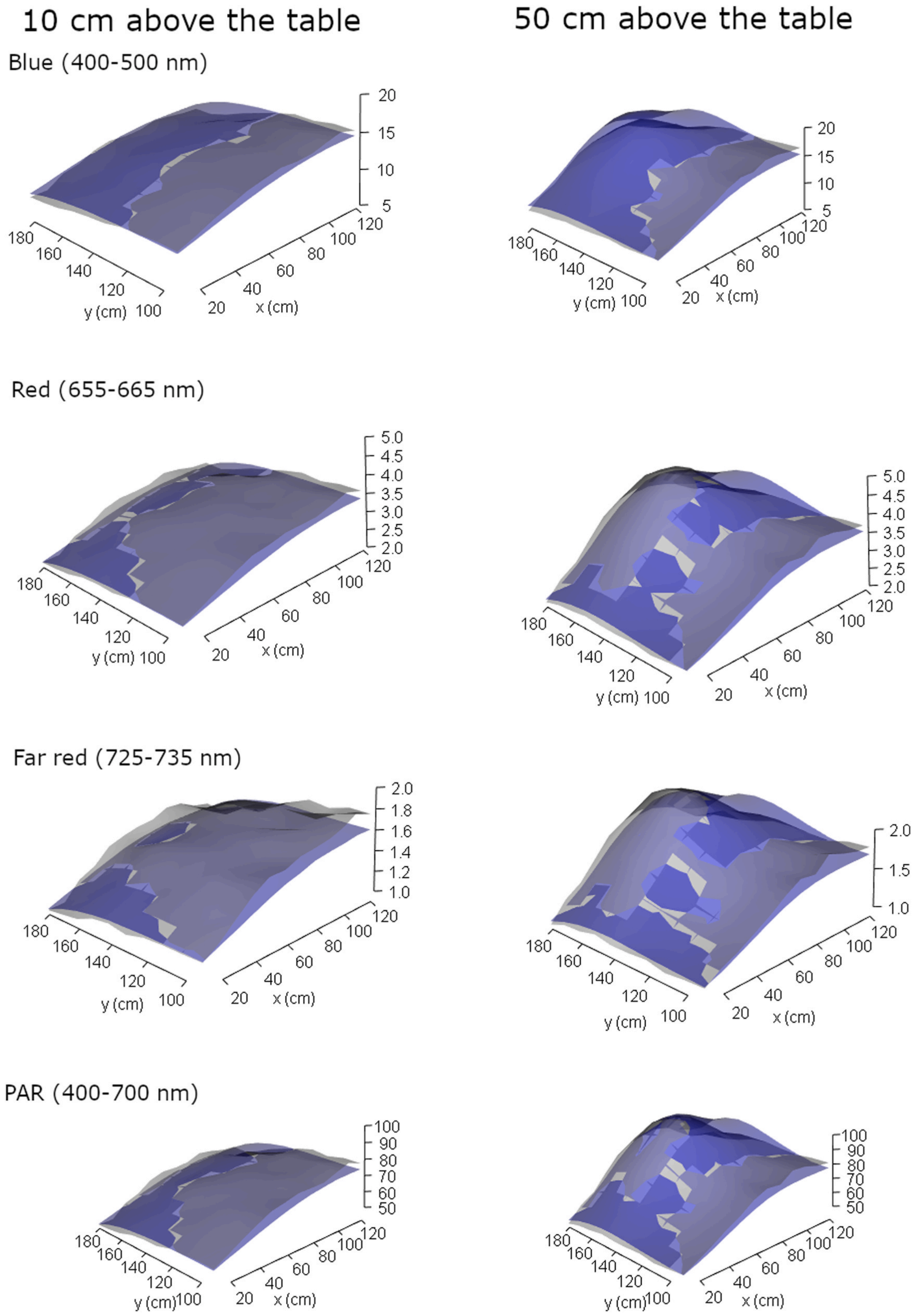

Fig. 7. Irradiance spatial variability in the growth chamber without plants. Simulated and measured irradiance (z axes) for different wavelengths of physiological interest according to the position in the growth chamber in Exp.1 at two heights: 10 cm (left column) and 50 cm (right column) above the table. The light grey surface represents the measured irradiance, the light blue surface the simulated irradiance. The surfaces are transparent, thus dark blue areas correspond to measurements below simulations, and dark grey areas indicate measurements above simulations. (For interpretation of the references to colour in this figure legend, the reader is referred to the Web version of this article.)

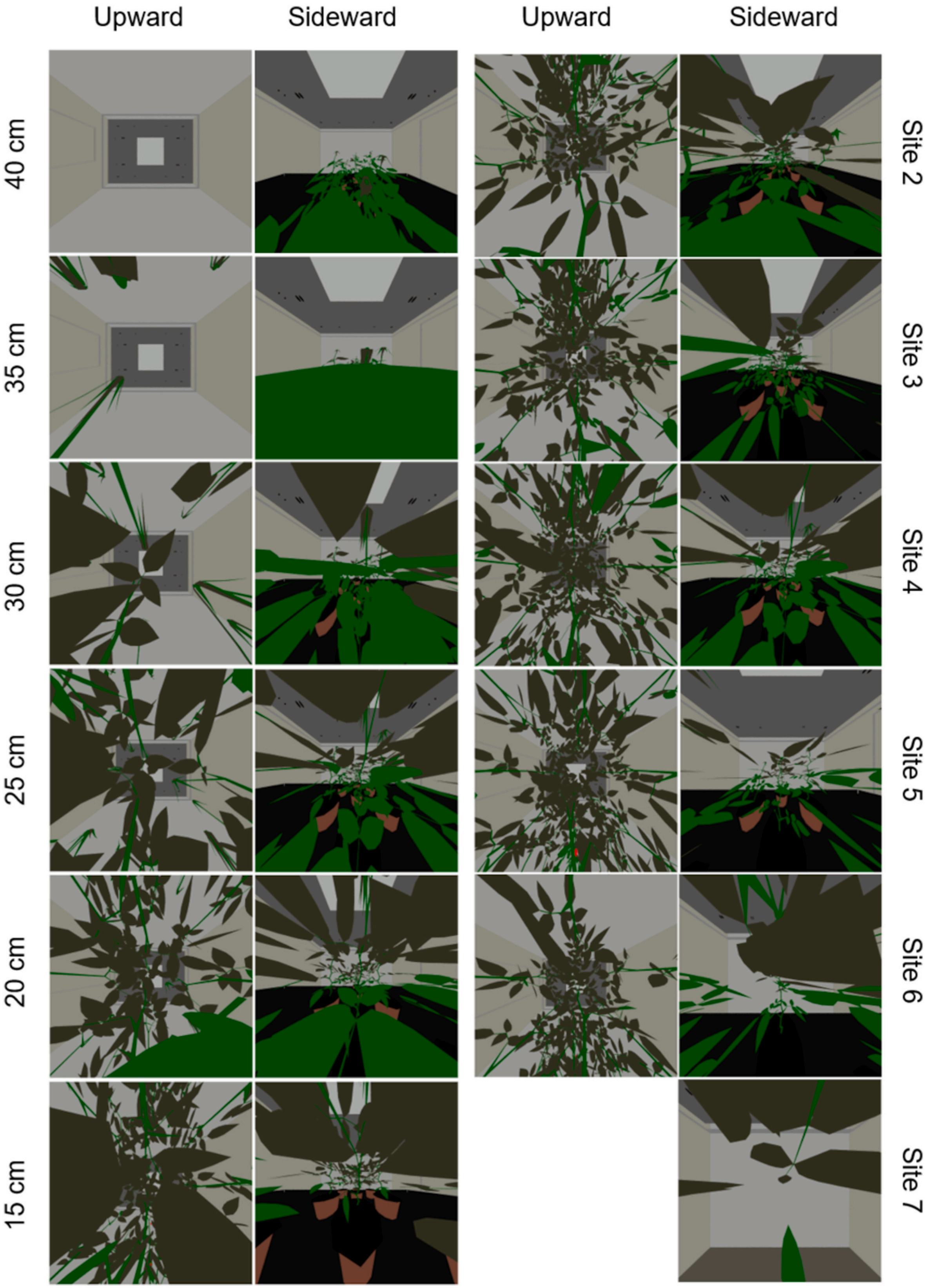

Fig. 8. Scene perception by a sensor moving within the plant canopy in Exp. 2. (**A**) Vertical movement from 15 cm above the table to above the canopy top (40 cm), and (**B**) horizontal movements from measurement sites 2 to 7 or 6. The sensor points upward or sideward toward the wall in front of site 7. The adaxial face of the leaves is represented in green, the abaxial face in dark grey, the stems and sepals are in green, the pots in brown, the table in black, and the elements of the growth chamber in lighter grey than the abaxial face of leaves. (For interpretation of the references to colour in this figure legend, the reader is referred to the Web version of this article.)

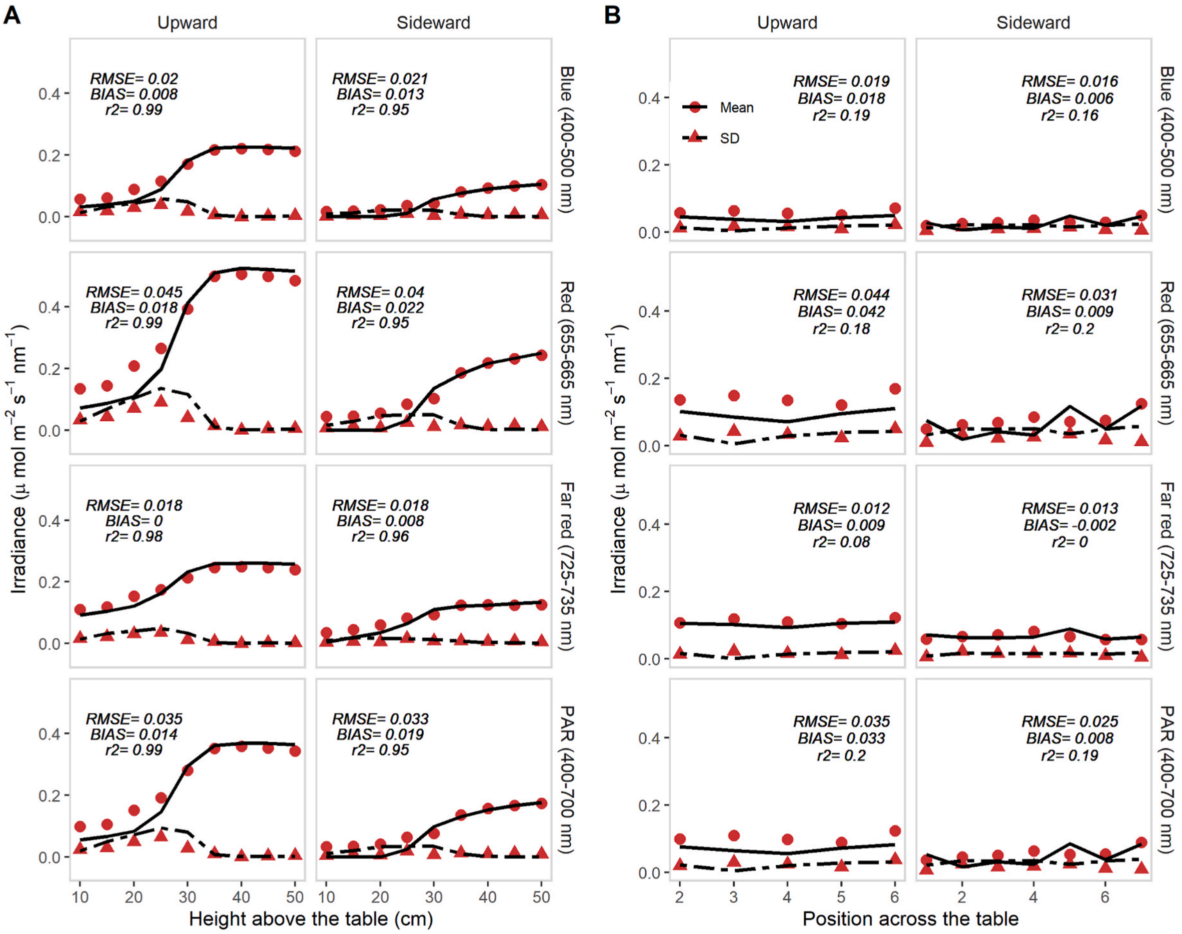

Fig. 9. Quality of the simulations within the plant canopy. Simulated (black lines) vs. measured (red symbols) mean irradiance (circles, full lines) and standard deviation (sd; triangles, dashed lines) between the five plant configurations in Exp. 2, for different wavelengths of physiological interest when light sensors are pointing either upward or sideward, and are travelling in the canopy either vertically from 10 to 50 cm above table (**A**) or horizontally from measurement site 1 to 7, or 2 to 6 (**B**). Irradiance is expressed by nm so as to allow the comparisons of wavebands of different widths. The full lines were built from linear interpolation between points simulated at the same positions as the measurement points. RMSE, Bias and r^2 are calculated for the mean irradiance. (For interpretation of the references to colour in this figure legend, the reader is referred to the Web version of this article.)

Despite the adequacy in the general trends of simulated and measured irradiance patterns, there were discrepancies in absolute values especially in the lower part of the canopy. Along the vertical transect (Fig. 9A), if the overall accuracy was good in blue and far-red wavebands (Blue: RMSE = 0.02 and 0.021, Bias = 0.008 and 0.013, for upward and sideward sensors, respectively; Far-red: RMSE = 0.018, Bias = 0 and 0.008 for upward and sideward sensors, respectively), the irradiance in the low part of the canopy was however under-estimated for all wavebands, and especially in the red and PAR, which are two wavebands simulated with lower accuracy (Red: RMSE = 0.045 and 0.04, Bias = 0.018 and 0.022, for upward and sideward sensors, respectively; PAR: RMSE = 0.035 and 0.033, Bias = 0.014 and 0.019, for upward and sideward sensors, respectively). This was accompanied for these bands by an over-estimation of the irradiance variability in the middle-low part of the canopy. Along the horizontal transects (Fig. 9B), mean irradiance values were generally underestimated, especially for the red and PAR wavebands with upward-pointing sensors, which is consistent with the under-estimation observed in the low part of the canopy along the vertical transect.

3.3. *Enhancement of simulated irradiance accuracy after measurement bias correction*

It is hypothesised that the lower accuracy in the lower part of the canopy could be caused by measurement inaccuracies when the sensors receive a high fraction of grazing irradiance (*i.e.* photons reaching the sensor with a high incidence angle), as the cosine corrector of our spectrophotometer may not be perfect, an assumption also previously made by Hitz et al. (2019).

The data used for calibration were a mix of sensors pointing upward, thus receiving photons with globally low incidence angle, and sensors pointing sideward, thus receiving photons with grazing incidence angles (Fig. S6, Supplemental Material). Under the assumption of imperfect cosine-corrector of the measuring probe, the calibration would give consistent simulations with the measurements only on the irradiance range on which it was established for each sensor orientation, respectively. In line with this assumption, simulations fitted well measurements in the top of the canopy, with irradiance values in the range of those measured without plants used for calibration (*e.g.* for blue waveband: 20 and 5–10 μmol m^{-2} s^{-1} for sensors pointing upward and sideward, respectively; Fig. 9 and Fig. S6, Supplemental Material), but were biased with respect to the observations in the lower part of the canopy, where irradiance values were slightly below the calibration range respectively to the sensor orientation.

To further test the role of the grazing irradiance in the deviations between simulations and measurements, two groups of sensor positions (all pointing upward) were compared, using Exp.1 data: (i) sensors in a horizontal plane close to the lamps (90 cm above the table) but with low values of irradiance (irradiance bellow the maximum at 50 cm), corresponding to sensors positioned far from the lamps and that were assumed to receive a high fraction of grazing irradiance, and (ii) the sensors previously used, positioned at 10 and 50 cm above the table (Fig. 5), that were assumed to receive lower fraction of grazing irradiance. The relationship between the raw simulations (number of photons per unit area) and the measured irradiance did not align for the two groups of data (Fig. 10). In contrast, if the sensors selected in the plane close to the lamps (90 cm above the table) had higher irradiance values—assuming that these sensors receive less grazing irradiance compared to those positioned farther away from the lamps—the two groups of data were aligned (Fig. S7, Supplemental Material). These results demonstrate a different calibration relationship for grazing and non-grazing light on sensors.

This measurement bias was eliminated by using independent calibrations for sideward- and upward-pointing sensors, to account for differences in light incidence on the two sensor groups (Fig. S8, Supplemental Material). The calibration lines were forced through the origin, as the variability of irradiance within each sensor group was low. The simulations fitted well to the observations, even at the bottom of the canopy (RMSE, between 0.011 and 0.038, bias between −0.032 and 0.0007; r^2 between 0.95 and 0.99 for vertical transects, near-zero r^2 values for horizontal transects were due to the stability of irradiance along these transects, Fig. 11). No systematic deviation was observed at the canopy edges, in front of the walls (positions 2 and 7, Fig. 11B). A detailed comparison between simulations and measurements, however, reveals a slight systematic overestimation at the bottom of the canopy for the upward-pointing sensors, and a slight systematic underestimation at the top of the canopy for the sideward-pointing sensors. This is likely to be related to calibration issues arising from the limited light range covered by the calibration points after separating the upward- and sideward-pointing sensors. For sideward-pointing sensors, the calibration line slightly overestimates the lowest measured values and underestimates those just above (e.g., between approximately 1.8 and 2.4 µmol m^{-2} s^{-1} for the red waveband, Fig. S8, dashed blue lines), and similar deviations could be at the origin of the deviations for upward-pointing sensors. In addition, local overestimations were observed at positions 1 and 5 of the horizontal transects, and at 30 cm in the vertical transect for sideward-pointing sensor. While the discrepancies between simulated and observed irradiance were generally of similar magnitude across the different wavelength bands throughout the transects, the errors at these specific positions were greater for red and PAR, strongly absorbed by leaves, than for blue and far-red. These overestimations are more difficult to interpret and could be related to reconstruction artifacts. For example, due to leaf positioning, a light gap in the canopy could have been simulated where none actually existed, an assumption consistent with the larger errors in wavelength bands that are strongly absorbed by leaves.

The patterns across the different transects of standard deviation for measured and simulated irradiance were highly consistent. However, upward-pointing sensors showed an overestimation at 30 cm in the vertical transect and an underestimation at site 3 (at 10 cm) in the horizontal transect. These inaccuracies affected all four wavelength bands, with greater discrepancy in the Red and PAR. Overall, the variability in irradiance within the canopy was accurately simulated.

Thus, with a calibration of the simulations on a few well-chosen calibration points, the model provides accurate simulations of the irradiance spatial variability within a canopy. This was shown for various sensor orientations and for the variability induced by different plant architectures at a single location, across different wavelengths with contrasted band widths.

3.4. *Light simulation indicates that increased interception by lower leaves and stem may stimulate bud outgrowth after temporary light limitation in rose*

To highlight the potential offered by this type of model in a growth chamber, an experiment was carried out in which branching —a plant development process highly sensitive to light—was unexpectedly affected by the application of different light intensities at an early stage of development. Previous data showed that a temporary light limitation during the development of one-axis rose plants, before the floral bud was visible at the top of the axis ("FBV" stage; Fig. 4), stimulates branching when plants return to high light intensity compared to a constant high light intensity (Demotes-Mainard, Huché-Thélier, et al., 2013). This was related to a stimulation of the outgrowth of axillary buds located at each leaf axil, a process initiating branches. These observations are particularly intriguing because low light intensity usually represses branching in rose (Corot et al., 2017; Wubs et al., 2014). Moreover, in this particular case, branching was stimulated while plants were under the same light intensity (light was reduced only before the branching period) indicating a role of the plant's light exposure history.

To better understand this unexpected behaviour, the original experiment of Demotes-Mainard, Bertheloot, et al. (2013) was reproduced, consisting of growing plants under early and temporary low PPFD (LH: Low-High) or under continuous high PPFD (HH: High-High). A subset of plants in both canopies was digitised (details in Material and Methods section), the entire canopy was reconstructed, and light was simulated for individual plants on which bud outgrowth was measured. Simulations were performed at two stages: just before and just after bud outgrowth period, coinciding respectively with FBV and PCV stages (Fig. 4A). At the times of simulation, all plants were exposed to high PPFD, in identical growth chambers. Light was simulated in PAR only, since branching is not responsive to blue or red:far-red ratio in this cultivar (Abidi et al., 2013; Crespel et al., 2020). The results shown in Figs. 12 and 13 represent the averages of architectural variables and light across the same individual plants.

As observed in Demotes-Mainard, Huché-Thélier, et al. (2013), bud outgrowth along the primary axis was stimulated for plants under LH modality. Under LH modality, all buds grew out whatever their position along the axis. In contrast, for HH modality the rate of bud outgrowth progressively decreased down the axis: 100 % for buds at relative rank 1 (calculation of relative rank in Materials and Methods section), to approximately 70 % for buds in the axil of a leaf at a median position on the axis (relative rank 0.5), to about 5 % for buds located in the axil of the lowermost leaf (relative rank 0) (Fig. 12A).

These data were compared with the architecture and light distribution along the primary axis of the same plants. An effect on the architecture of the primary axis bearing the buds, with overall larger organs in the LH modality compared to the HH modality, was observed. More specifically, the length of individual internodes was greater along the entire axis at FBV, while this difference was only visible in the lower two-thirds of the axis (relative rank <0.7) at PCV (Fig. 12B). The surface area of individual leaves was greater in LH modality in the lower half of the axis at both stages, while it was equal at FBV and even slightly smaller at PCV for leaves in the upper half (Fig. 12C). The cord length of the leaf rachis (Fig. S1 for details about the cord) was greater in LH modality along the entire axis at FBV and in the lower half of the axis at PCV (Fig. 12D).

These differences in architecture led to significant differences in light distribution along the axis. Internodes of LH plants intercepted a significantly higher quantity of irradiance per unit surface than those of HH plants at both FBV and PCV stages, regardless of their position on the stem, although plants of both modalities were subjected to the same incident light at the time of light simulations (Fig. 13). For leaves, only lower leaves at FBV (relative rank <0.25) displayed higher irradiance interception for LH compared to HH modality, whereas upper leaves at PCV displayed lower interception in LH. In conclusion, these data show that despite identical incident light at the time of bud outgrowth, bud outgrowth and thus branching was stimulated in a modality in which plants experienced early-stage light restriction. This stimulation was correlated with a modification of the architecture of the axis bearing the buds, leading to an increase in irradiance received by the stem and basal leaves, which could therefore be the cause of the observed branching

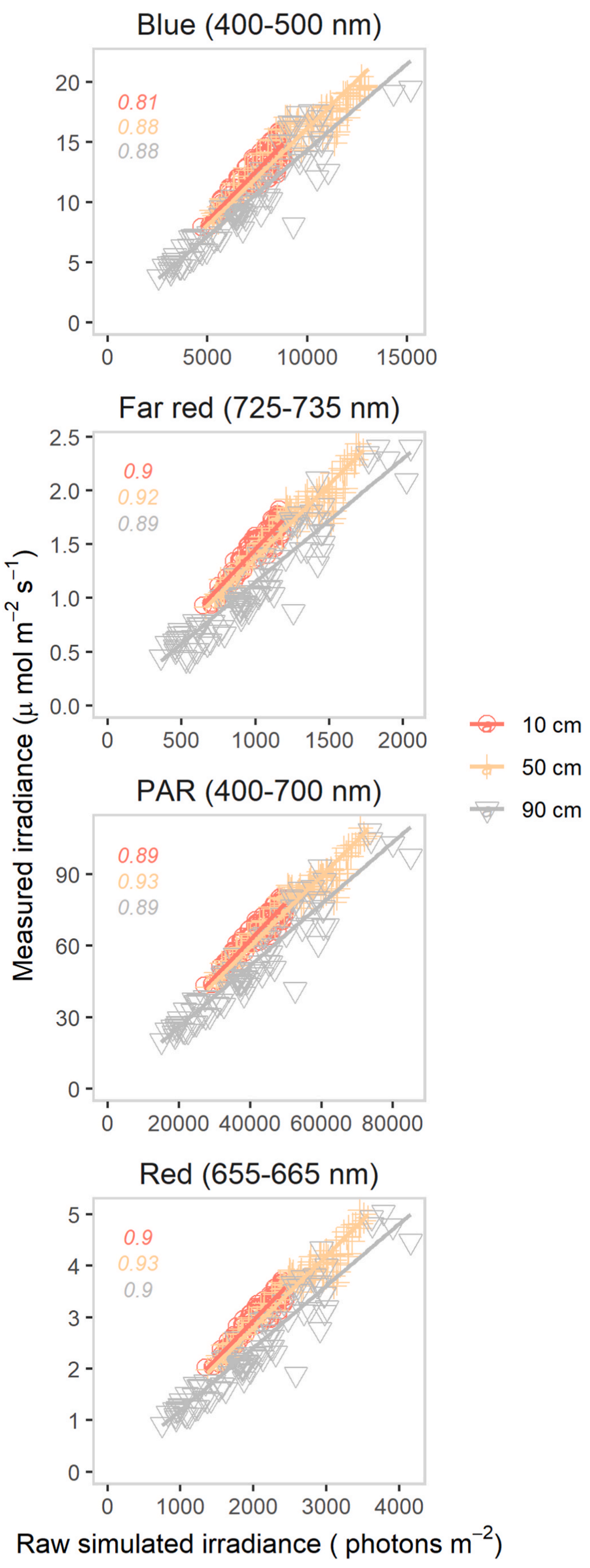

(caption on next column)

Fig. 10. Comparison of simulation and observation relationships at varying light incidence angles in Exp. 1. Data from 10, 50 and 90 cm above the table are shown. At 90 cm, only points with irradiance bellow the maximum at 50 cm are included, indicating that the light at 90 cm has a more grazing incidence than at 50 cm or 10 cm. Lines represent linear regressions; coloured numbers indicate r^2 values for 10 (red), 50 (orange), and 90 cm (grey). (For interpretation of the references to colour in this figure legend, the reader is referred to the Web version of this article.)

stimulation after temporary light restriction. If leaves could act by increasing sugar availability for the buds, a major stimulator of bud outgrowth, the role of light perceived by the stem remains unknown and would definitively deserve further investigation.

4. Discussion

Light models in general and ray-tracing models in particular offer the possibility to estimate light quantity and quality intercepted by the organs of plants growing in growth chambers, and thus analyse the response of crops whether in experimental or production conditions (Hitz et al., 2020; Kahlen & Stützel, 2011; Sarlikioti, de Visser, Buck-Sorlin, & Marcelis, 2011; Sarlikioti, de Visser, & Marcelis, 2011; Zhang, van Westreenen, Anten, Evers, & Marcelis, 2020). This work provides a detailed description of how to use a ray tracing model in a growth chamber and, in particular, proposes a calibration method that takes into account the intensity and quality of the light sources, and rationalises the number of measurement points in the growth chamber according to its configuration. This method makes it possible to accurately estimate light distribution on vertical and horizontal plant organs at different locations within a canopy. Results focused on physiologically important wavebands of differing widths, for which the optical properties of the leaves vary. The efficacy of the model for biological investigations is exemplified using the case study of light regulation of branching in rose plants.

4.1. The reproduction of the growth chamber, light emission sources and plants

To provide insight into the light phylloclimate at different wavelength bands, a series of steps were undertaken to virtually reproduce the real scene (growth chamber and plants) and simulate photon fluxes. As a preliminary step, it was ensured that a sufficient number of photons were launched to guarantee the reproducibility of the results, as ray-tracing models are based on a Monte Carlo strategy.

To reproduce the real scene, the first step involved the virtual reconstruction of the growth chamber, including the characteristics of its materials, and the canopy, as is typically done in light simulation studies. For the growth chamber, the reconstruction was based on the representation of the main elements of the chamber (floor, walls, tabletop, translucent panel separating the compartments, lamps, baffles and ceiling) and of the heterogeneous components as uniform components (the multicellular translucent panel separating the lamps from the crop compartment, the perforated lateral walls). The overall accuracy of the simulations shows that these simplifications are permissible. The regular spacing of the holes in the studied perforated metal wall, the high number of rays, and the fact that the reflectance values account for the holes (Materials and Methods), suggest a minimal effect. Additionally, Saito et al. (2020) also modelled a metallic perforated surface as a uniform component with average reflectance. Moreover, the simulations were only slightly sensitive to the reflectance of this wall (see below). Representing the multicellular translucent panel as a homogeneous material may have introduced inaccuracies, particularly because the simulations were sensitive to its transmittance (see below). A visually evident preferred direction of light along the axis of these cells could have contributed to errors in the simulations.

Optical properties were attributed (i) for each material present in the

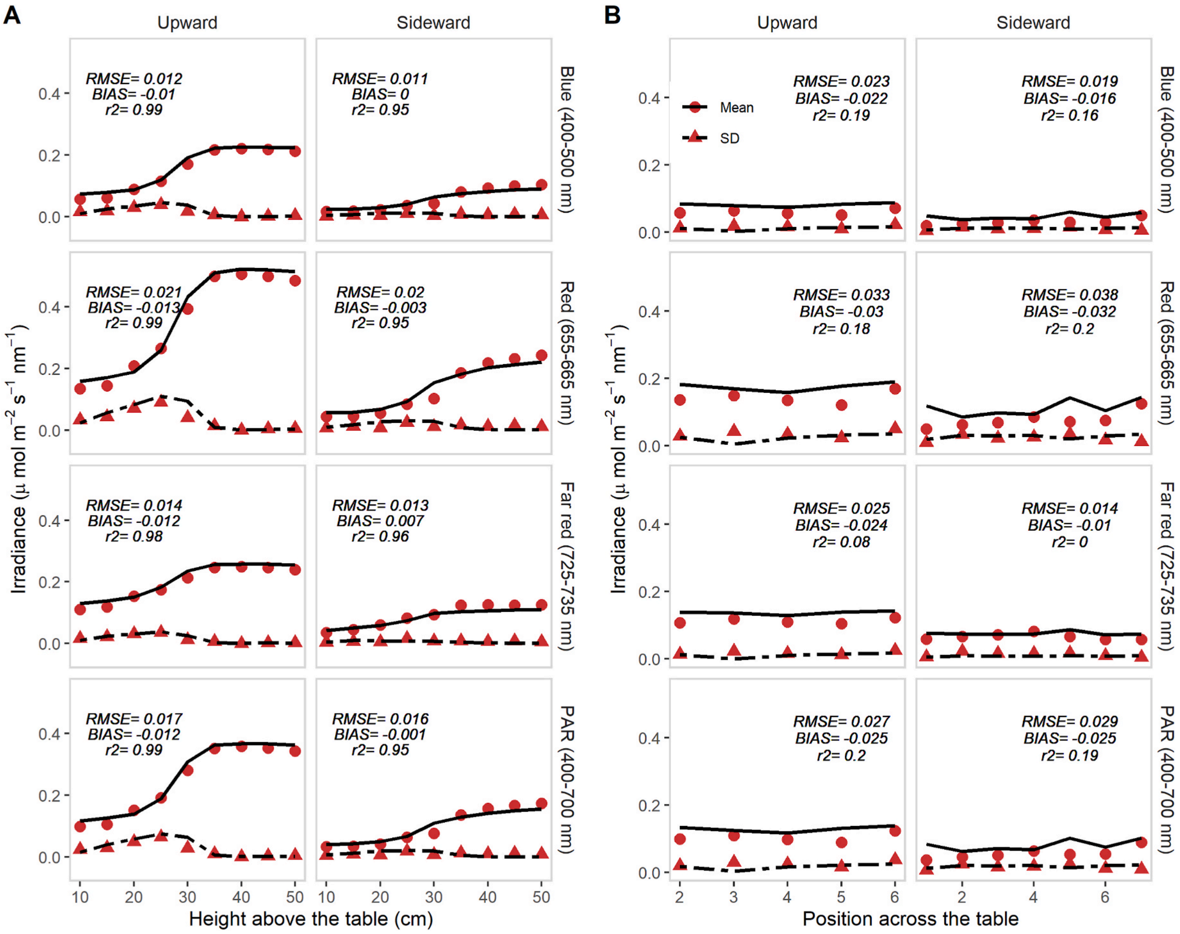

Fig. 11. Quality of the simulations within the plant canopy, after correction for measurement bias. Simulated (black lines) vs. measured (red symbols) mean irradiance (circles, full lines) and standard deviation (sd; triangles, dashed lines) between the five canopy configurations in Exp. 2 for different wavelengths of physiological interest when light sensors are pointing either upward or sideward, and are travelling in the canopy either vertically from 10 to 50 cm above table (**A**) or horizontally from measurement sites 1 to 7, or 2 to 6 (**B**). Irradiance is expressed by nm so as to allow the comparisons of wavebands of different widths. The full lines were built from linear interpolation between points simulated at the same positions as the measurement points. RMSE, Bias and r^2 are calculated for the mean irradiance. (For interpretation of the references to colour in this figure legend, the reader is referred to the Web version of this article.)

chamber and for plant elements, to take into account the specific effect of each element on light fluxes, and (ii) according to the waveband considered to account for the variations of optical properties between wavebands. For plants, the optical properties of the adaxial and abaxial leaf surfaces, as well as the differences between folded ('young') and fully opened ('mature') leaves were considered because these characteristics affect the reflectance and transmittance (Noda, Muraoka, & Nasahara, 2021). However, variations in age and position within the canopy among mature leaves were not accounted for. Since all leaves appeared within approximately 9–14 days on a primary axis, differences in optical properties among leaves of different ages are likely minimal. Nonetheless, for longer experiments it may be necessary to refine the optical properties of leaves, as age and light exposure cause changes throughout the season (Noda et al., 2021). Accurate optical property values are important since they affect light simulations, depending on the material and its position within the chamber. For instance, a ±10 % variation in the reflectance of the shiny metal (located in the lamp compartment and which notably includes the baffles) resulted in an average variation of ±7 % in the photons m-2 intercepted by the sensors in Exp. 1. Similarly, a ±10 % variation in the transmittance of the multicellular panel led to a variation of ±11 % photons m-2. In contrast, a ±10 % variation in the reflectance of other materials had a minor impact, with variations of ±2.5 % for the perforated brushed metal wall, ±1.7 % for the white wall, and ±1 % for the multicellular panel.

The second step was to reproduce emission sources, which includes accounting for the photometric volume, *i.e.* the irradiance distribution around the lamp, as well as light sources intensity and quality (spectrum). A realistic photometric curve was easily obtained from the reproduction of lamp geometry. This provides an alternative to the direct integration of the photometric curve proposed in other studies (Henke & Buck-Sorlin, 2017; Saito et al., 2020). The strategy adopted here for accounting for variations in light intensity and spectrum was to make these adjustments a posteriori, after completing simulations. Thus, for a lamp, the same number of photons was launched for each waveband, whatever its width and lamp irradiance in this band. The heterogeneity of the spectrum was accounted for by weighing the number of photons simulated in each band and intercepted by each sensor, by the proportion of irradiance emitted by the lamp in that band. This method, compared to a method that directly set lamp spectrum as input of the light model, ensures that enough photons are launched, even in narrow bands (*e.g.* the red and far-red 10 nm bands) and in the troughs of the spectrum. To account for the intensity of the lamp, the number of simulated photons in each band was converted into irradiance based on the observed linear relationship between photon number and irradiance on sensors placed at several locations in the empty growth chamber.

4.2. *Reproduction of irradiance distribution in a growth chamber from a limited number of well-chosen irradiance measurements*

To calibrate the model on irradiance measurements, the possibility of

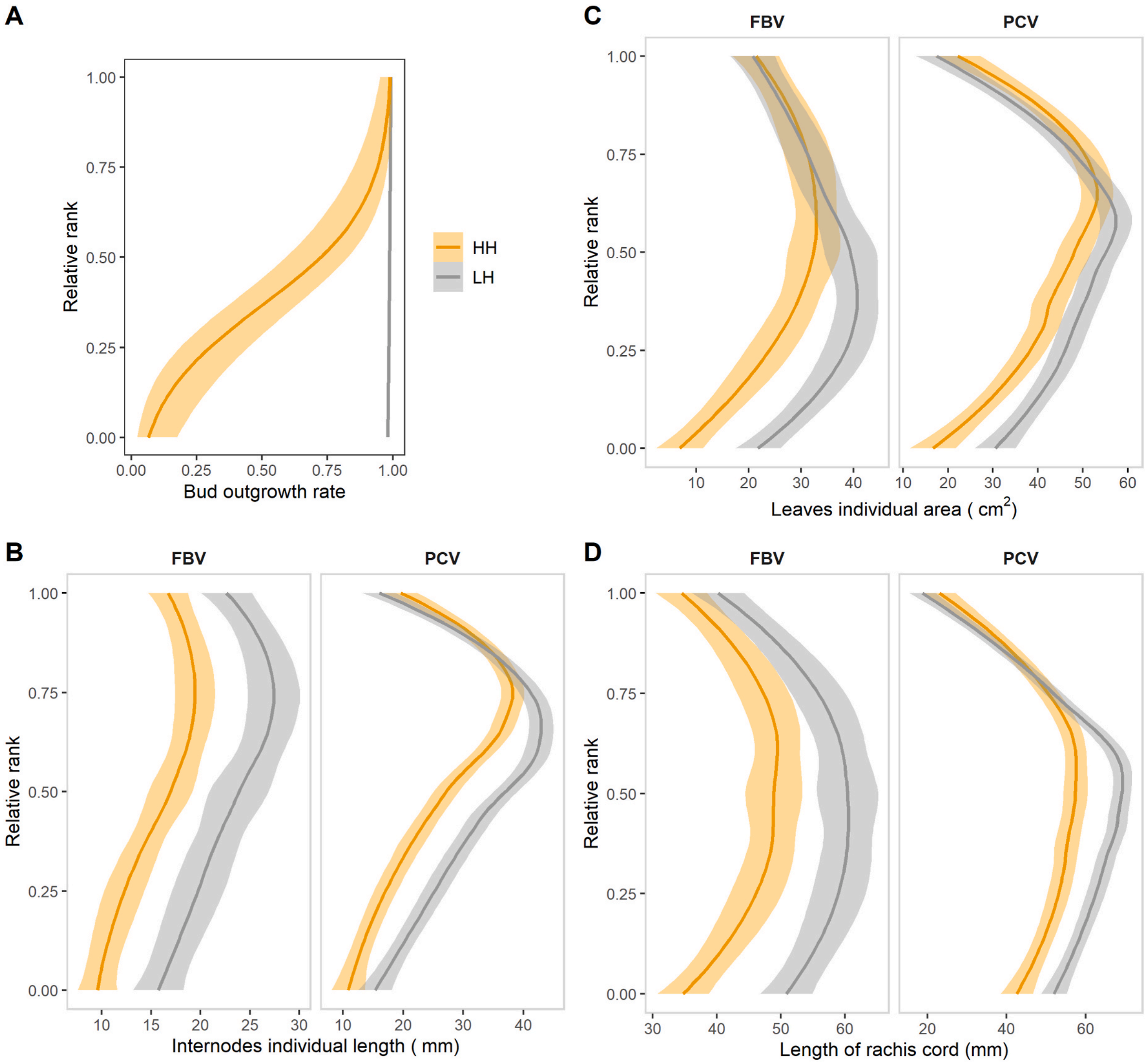

Fig. 12. Architectural description of rose plants grown under continuous high PPFD (HH) or after temporary PPFD limitation (LH). Bud outgrowth rate at different ranks on the primary axis few days after PCV stage **(A)**, and corresponding architecture of the primary axes: internode length (excluding peduncle) **(B)**, leaf area **(C)**, and length of the cord of leaf rachis **(D)**. Means are shown (dark lines) with 95 % confidence intervals (light-coloured areas).

using a limited number of sensors chosen according to chamber configuration is demonstrated. Sensors are located in the zone of culture to optimise the chances of capturing existing variability in the growing zone, and positioned so as to vary the distance from the lamps and walls, elements likely to exert a major influence on irradiance variability in the empty chamber. In case of different types of walls, the distance from each type of wall is varied to take into account potential effects linked to their specific optical properties. The choice of several sensors rather than only one relies on the existence of a variability around the regression between simulations and measurements. This overall strategy provides an accurate simulation of irradiance, as illustrated in the first experiment (at 10 and 50 cm above the culture table with upward-pointing sensors; Fig. 6 and Fig. S5). It has been considered in a generic manner to be applicable in other growth chambers, and evaluating its performance in different growth chambers with varying geometries and material optical properties would be the next step. If the range of irradiance obtained using this strategy is too low to establish a calibration line accurately, it is possible to force the calibration line by the origin. Indeed, in Exp. 1 the intercept between simulations and measurements were significantly different from zero but close to zero, as also reported by Hitz et al. (2019), and Kim et al. (2020). In the case of a chamber having dimmable LEDs, it would be possible to generate an intensity range to establish this calibration line.

Using this strategy, sensor positions should be chosen to avoid pointing away from the lamps, as this can lead to grazing incidence, which the cosine corrector of the measurement probe is likely to handle inaccurately. When irradiance was grazing (such as with the sensors in Exp. 2 pointing sidewards or in Exp. 1 at positions laterally offset from the lamps at a height of 90 cm above the table) the linear relationship between simulations and measurements differed from that observed for sensors receiving non-grazing irradiance (Fig. 10). This difference was attributed to biases in the measurement of grazing irradiance. Such bias has already been suggested by Hitz et al. (2019) to explain a lower accuracy in simulations for sensors pointing away from the lamps. Zhang, Henke, et al. (2020) also hypothesised measuring problems to explain discrepancies between simulated and measured global radiation at low solar elevation angles in a greenhouse. In this work, including sensors receiving grazing irradiance (sensors pointing sideward) to calibrate the model in Exp. 2 led to significant discrepancies between simulations and measurements in the low part of a rose canopy (Fig. 9).

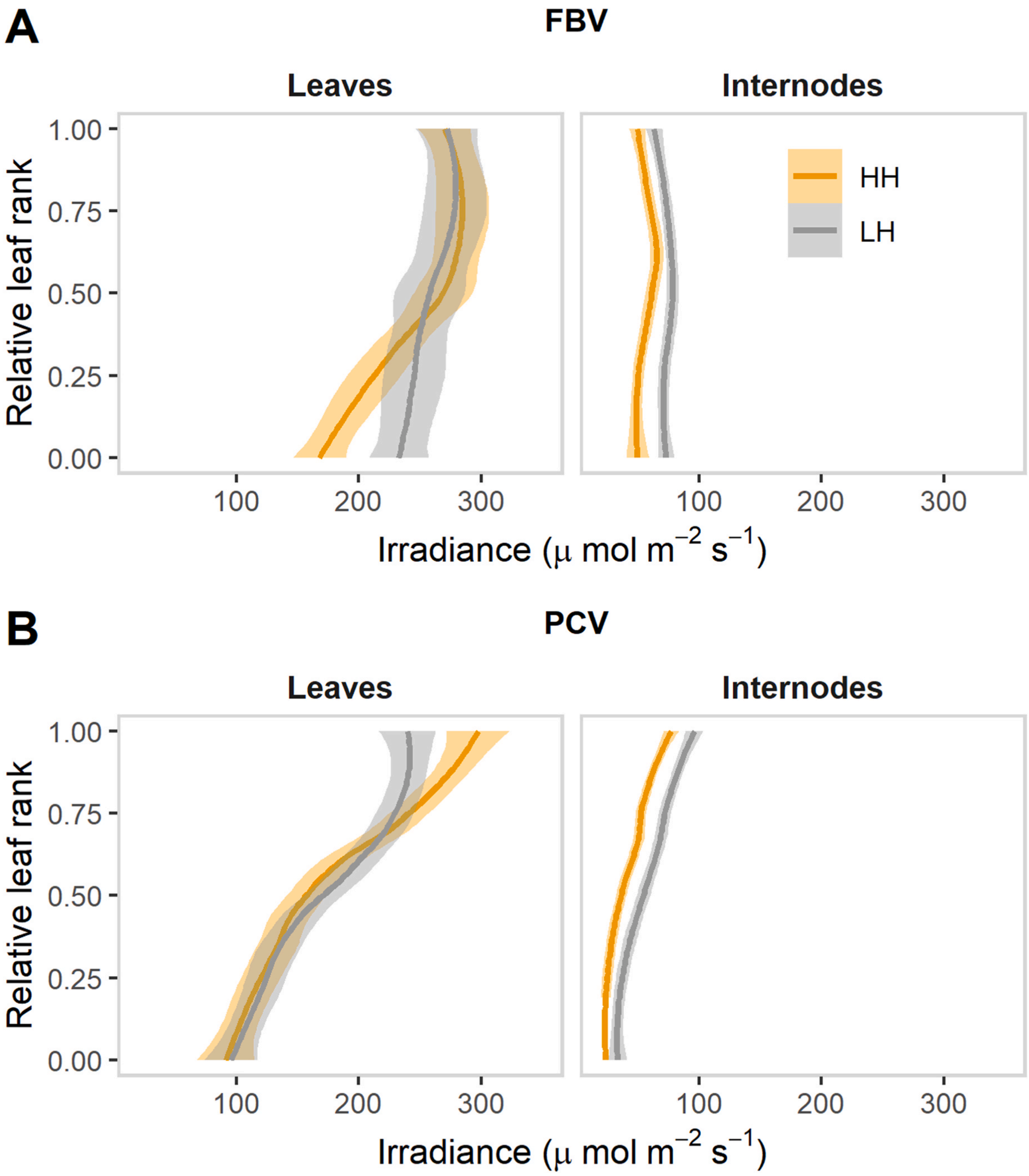

Fig. 13. Irradiance distribution along axes of roses grown under continuous high PPFD (HH) or after temporary PPFD limitation (LH). Simulated irradiance intercepted by leaves and internodes along the axis at FBV **(A)** or PCV stages (**B**). All plants were exposed to high PPFD at the time of simulation. Means are shown (dark lines) with 95 % confidence intervals (light-coloured areas).

4.3. Accurate simulations in different wavebands when progressing horizontally and vertically in a canopy with different sensor orientations

The whole operating procedure enables reproducing irradiance distribution in the growth chamber and within a canopy in different wavebands of physiological interest: blue (400–500 nm), red (655–665 nm), far red (725–735 nm), and PAR (400–700 nm). This extends previous conclusions for growth chambers in the absence of plants, where accurate simulations were observed in PAR and in four 100 nm-width wavebands using ray-tracing models (Hitz et al., 2019; Kim et al., 2020; Lee et al., 2023; Saito et al., 2020). This work demonstrates a good level of accuracy in a larger and more complex growth chamber, due to the diversity and heterogeneity of its materials, as well as for more contrasted waveband widths.

The evaluation of light simulations using ray tracing models is scarce in literature when applied in a scenario with plants growing in the chamber and is limited spatially and in terms of wavebands. In a greenhouse, a high correlation was reported between simulations and measurements in PAR at different heights within a cut-flower rose canopy with upward-pointing sensors, but at a large spatial scale (the observation unit was the average of 50–100 upward pointing sensors of 5 cm radius) (Buck-Sorlin et al., 2011). In growth chambers, a high correlation was reported between simulations and measurements with upward pointing sensors below a lettuce canopy in the PAR, and at an intermediate height of four soybean plants canopies in a 100 nm-width waveband (Hitz et al., 2018; Kim et al., 2020). This study goes further by demonstrating for the first time that light gradients caused by varying the distance to the lamps and to the walls, that adds to the usual gradients generated by light attenuation with canopy depth, are accurately simulated. Indeed, the observed patterns of irradiance, while penetrating vertically or horizontally in the canopy, are reproduced. This good behaviour is observed for wavebands of different widths and two sensor orientations. The quality of the prediction is comparable for wavelength bands that are both strongly and weakly absorbed by the canopy. Plant organs exhibit a wide range of angles; the similar accuracy achieved with both upward- and sideward-facing sensors supports the assumption that the simulations would also be accurate for other angles. In addition, it is demonstrated that the variability of irradiance when plant architecture varies, and not only its mean, is accurately simulated. Thus, the irradiance perceived by the plant organs within a canopy can be assessed with a correct confidence interval around the mean. This property is important for biological studies that investigate the functioning of plants at the canopy scale. It makes it possible to compare statistically the irradiance experienced by different canopies with contrasting architectures, as in Exp. 3. Consistently, using a radiosity based model, the variability in PAR induced by sky conditions and time of the day was reproduced inside cucumber canopies grown in a greenhouse (Wiechers et al., 2011).

This evaluation was conducted within a small and sparse canopy. In a dense canopy, it would be essential to be aware of the risk in the PAR of launching too few photons to sample all the small gaps in the foliage through which light may penetrate. Additionally, in the far-red range, it would be crucial to account for the high levels of light scattering generated in dense canopies. With ray-tracing models it necessitates permitting sufficient photon bounces. Future steps to reduce uncertainty, may involve advanced optical measurements, including the characterisation of the bidirectional reflectance distribution function (BRDF) and the bidirectional reflectance transmittance function (BRTF) of materials, as well as multi-layer modelling of leaves (Bailey et al., 2014).

4.4. Using light simulation and plant architecture reconstruction to hypothesise rose responses to light

Using the light simulation environment, hypotheses could be formulated to explain the previously observed stimulation of bud outgrowth, the initial process of branching, following an early and temporary limitation in incident light (LH) in rose (Demotes-Mainard, Huché-Thélier, et al., 2013). This behaviour is counter-intuitive because light limitation usually impairs bud outgrowth (Corot et al., 2017; Wubs et al., 2014). The results indicate that this behaviour was associated with an increase in light interception per unit area of the basal leaves and the stem’s surface area along its entire length. This was observed compared to a modality where light was maintained at a higher level throughout plant growth (HH), and this despite similar incident high light intensity (420 μmol m^{-2} s^{-1} at 30 cm above the culture table) in both modalities during bud outgrowth period. Early light limitation induced architectural changes in the plant, particularly longer internodes and rachises, that might have reduced vertical light attenuation. Several studies have focused on the effect of light on bud outgrowth, highlighting both the role of sugar availability and hormones such as cytokinins, which are inducers of bud outgrowth (Schneider et al., 2019; Wang et al., 2021). Both regulators may be involved in the present study. Sugar availability may have increased due to the observed rise in light interception by the basal leaves, which are mature and therefore function as photosynthetic organs that export sugars. In addition, the area of these leaves was greater in LH modality, enhancing the surface area for light interception and further increasing photosynthesis (Fig. 12C). However, the regulation of sugar availability in plants depends not only on photosynthesis but also its balance with the sink organs (here, young leaves, internodes and floral bud) that require sugar for their growth. Consequently, quantifying this balance and conducting more detailed studies are necessary to draw further conclusions. Regarding the increase in light intercepted by the stem, the role of the stem as a light sensor in the control of bud outgrowth has yet to be demonstrated. Decapitated and defoliated rose stems exposed to light, experience increased bud outgrowth compared to plants kept under darkness, and stimulation of cytokinin production in the nodes is reported to play a role (Roman et al., 2016). Similarly, low levels of cytokinins in the internodes have been associated with the inhibition of bud outgrowth in intact plants grown under low incident light intensity compared to those grown under higher light intensity (Corot et al., 2017). Therefore, the significant role of light intercepted by the stem and associated cytokinins cannot be excluded and warrants further investigation. This discussion, using the regulation of branching by light as a case study, underscores the usefulness of a robust light simulation framework in formulating hypotheses to explain counter-intuitive plant behaviours, and demonstrates the value of light simulation tools for experiments in growth chambers and guiding future studies in plant biology research.

In this study, the capabilities of the light simulation tool to investigate a biological process were limited by time-constraints associated with the laborious digitalisation of plant architecture. This resulted in a limited number of light simulation points during plant growth and hindered a detailed exploration of the relationship between intercepted light and bud response, acknowledging that the bud response to light is unlikely to be instantaneous but probably results from an integration over time. However, tools are currently being developed to automatically reconstruct plants in 3D from images, allowing for dynamic monitoring of plant architecture (Artzet et al., 2019; Daviet, Fernandez, Cabrera-Bosquet, Pradal, & Fournier, 2022). Coupling these tools with ray-tracing models in growth chambers would allow continuous estimation of light interception by organs throughout plant growth, giving the possibility to investigate plant response to light phylloclimate in a more dynamic way. Further advancements could also be made by modelling plant functioning processes, such as the relationships between source and sink organs for carbon within the developing and reconstructed plant architecture. Such models have been developed for various species (Evers et al., 2010; Luquet, Dingkuhn, Kim, Tambour, & Clement-Vidal, 2006; Mathieu, Cournède, Letort, Barthélémy, & de Reffye, 2009), and their coupling with a light simulation tool in a growth chamber would enable a more in-depth exploration of hypotheses concerning non-intuitive plant responses. Real-time modelling could also better account for potential fluctuations in light environment, such as those resulting from material or lamp aging, which may be crucial for use in long-duration crops or successive cropping cycles, such as those in vertical farms.

5. Conclusion

Ray-tracing models are a valuable tool for estimating the light phylloclimate of crops grown in growth chambers, which are inherently anisotropic environments. Accurate estimations of light intercepted by plant organs are largely dependent on how these models are used. A generic method to identify the necessary irradiance measurement points for reliable simulation is detailed herein. Additionally, a method is proposed to account for the intensity and spectrum of light emission sources, with these factors addressed after completing the simulations. Using these methods, this work demonstrates the reliability of ray-tracing models, exemplified by the SEC2 framework, in providing insights into the phylloclimate across different wavebands of physiological interest and organ orientations, a major determinant of morphogenesis and photosynthesis. Both the mean irradiance at different positions within a canopy and the variability induced by plant architecture are accurately simulated, thus allowing analysis of the response of canopies in growth chambers for both experimental and production purposes. Environments in growth chambers can alter light phylloclimate both directly, such as through changes in incident light, and indirectly, by affecting plant architecture. In this study, the latter effect is illustrated in the case of light control of rose branching, in which over-stimulation following temporary light limitation was correlated to an increase in irradiance intercepted by the lower leaves and the entire stem, linked to changes in plant architecture. Looking ahead, the next steps would be to integrate the results of this work into an intuitive software tool to promote the wider adoption of ray-tracing models.

CRediT authorship contribution statement

Sabine Demotes-Mainard: Writing – review & editing, Writing – original draft, Visualization, Supervision, Project administration, Methodology, Funding acquisition, Conceptualization. **Hervé Autret:** Writing – original draft, Visualization, Software, Investigation, Data curation. **Christophe Pradal:** Writing – review & editing, Software, Resources, Data curation. **Julien Le Gall:** Writing – review & editing, Methodology, Investigation, Data curation. **Vincent Guérin:** Writing – review & editing, Supervision, Funding acquisition, Conceptualization. **Nathalie Leduc:** Writing – review & editing, Supervision, Project administration, Funding acquisition. **Didier Combes:** Writing – review & editing, Supervision, Resources. **Christophe Renaud:** Writing – review & editing, Supervision, Software, Resources, Data curation. **Michaël Chelle:** Writing – review & editing, Supervision, Resources, Conceptualization. **Jessica Bertheloot:** Writing – review & editing, Writing – original draft, Visualization, Validation, Supervision, Project administration, Methodology, Formal analysis, Conceptualization.

Declaration of generative AI and AI-assisted technologies in the writing process

During the preparation of this work the authors used ChatGPT in order to improve language and readability. After using this tool/service, the authors reviewed and edited the content as needed and take full responsibility for the content of the publication.

Funding

This work was supported by the Institut National de Recherche pour l'Agriculture, l'Alimentation et l'Environnement (INRAE, French National Research Institute for Agriculture, Food, and Environment); and by the French Region Pays de la Loire.

Declaration of competing interest

The authors declare that they have no known competing financial interests or personal relationships that could have appeared to influence the work reported in this paper.

Acknowledgements

We thank Gérard Sintès and Gilles Guillemain (UMR IRHS) for help with spectral measurements, Odile Douillet (UMR IRHS) for assistance with plant growth, Bruno Andrieu (UMR EcoSys) for fruitful scientific discussions, Kristian Johnson for his help in improving the English of this manuscript, and Aurélien Besnier for creating the package for 3D reconstruction and the documentation. Christophe Pradal has been supported partly by CIRAD's MaCS4Plants network and the European PHENET programme (PHENET, project No. 101094587 - Tools and methods for extended plant PHENotyping and EnviroTyping services of European Research Infrastructures).

Appendix A. Supplementary data

Supplementary data to this article can be found online at https://doi.org/10.1016/j.biosystemseng.2025.104256.

References

Abidi, F., Girault, T., Douillet, O., Guillemain, G., Sintes, G., Laffaire, M., et al. (2013). Blue light effects on rose photosynthesis and photomorphogenesis. *Plant Biology, 15*, 67–74. https://doi.org/10.1111/j.1438-8677.2012.00603.x

Artzet, S., Chen, T. W., Chopard, J., Brichet, N., Mielewczik, M., Cohen-Boulakia, S., et al. (2019). Phenomenal: An automatic open source library for 3D shoot architecture reconstruction and analysis for image-based plant phenotyping. https://hal.inrae.fr/hal-02788579.

Bailey, B. N., Overby, M., Willemsen, P., Pardyjak, E. R., Mahaffee, W. F., & Stoll, R. (2014). A scalable plant-resolving radiative transfer model based on optimized GPU ray tracing. *Agricultural and Forest Meteorology, 198–199*, 192–208. https://doi.org/10.1016/j.agrformet.2014.08.012

Boonen, C., Samson, R., Janssens, K., Pien, H., Lemeur, R., & Berckmans, D. (2002). Scaling the spatial distribution of photosynthesis from leaf to canopy in a plant growth chamber. *Ecological Modelling, 156*(2–3), 201–212. <Go to ISI>://000178386700008.

Buck-Sorlin, G., de Visser, P. H. B., Henke, M., Sarlikioti, V., van der Heijden, G. W. A. M., Marcelis, L. F. M., et al. (2011). Towards a functional-structural plant model of cut-rose: Simulation of light environment, light absorption, photosynthesis and interference with the plant structure. *Annals of Botany, 108*(6), 1121–1134. https://doi.org/10.1093/aob/mcr190

Chelle, M. (2005). Phylloclimate or the climate perceived by individual plant organs: What is it? How to model it? What for? *New Phytologist, 166*, 781–790.

Chelle, M., & Andrieu, B. (1998). The nested radiosity model for the distribution of light within plant canopies. *Ecological Modelling, 111*(1), 75–91. https://doi.org/10.1016/s0304-3800(98)00100-8

Chelle, M., & Andrieu, B. (2006). Modelling the light environment of virtual crop canopies.*Wageningen Ur Frontis Series* [Functional-structural plant modelling in crop production]. *Workshop on functional-structural plant modelling in crop production*. Wageningen, NETHERLANDS.

Chelle, M., Renaud, C., Delepoulle, S., & Combes, D. (2007). Modeling light phylloclimate within growth chambers. *5th international workshop on functional-structural plant models*. Napier (NZ).

Chenu, K., Rey, H., Dauzat, J., Lydie, G., & Lecoeur, J. (2008). Estimation of light interception in research environments: A joint approach using directional light sensors and 3D virtual plants applied to sunflower (Helianthus annuus) and Arabidopsis thaliana in natural and artificial conditions. *Functional Plant Biology, 35* (9–10), 850–866. https://doi.org/10.1071/fp08057

Corot, A., Roman, H., Douillet, O., Autret, H., Perez-Garcia, M.-D., Citerne, S., et al. (2017). Cytokinins and abscisic acid act antagonistically in the regulation of the bud outgrowth pattern by light intensity. *Frontiers in Plant Science, 8*(1724). Retrieved 2017-October-10, from https://www.frontiersin.org/article/10.3389/fpls.2017.01724.

Crespel, L., Le Bras, C., Amoroso, T., Unda Ulloa, M. G., Morel, P., & Sakr, S. (2020). Genotype x light quality interaction on rose architecture. *Agronomy, 10*(913). https://www.mdpi.com/2073-4395/10/6/913.

Daviet, B., Fernandez, R., Cabrera-Bosquet, L., Pradal, C., & Fournier, C. (2022). PhenoTrack3D: An automatic high-throughput phenotyping pipeline to track maize organs over time. *Plant Methods, 18*(1), 130. https://doi.org/10.1186/s13007-022-00961-4

de Visser, P. D., Buck-Sorlin, G., & van der Heijden, G. W. (2014). Optimizing illumination in the greenhouse using a 3D model of tomato and a ray tracer. *Frontiers in Plant Science, 5*(48). Retrieved 2014-02-18T00:00:00Z, from.

Delepoulle, S., Renaud, C., & Chelle, M. (2008). Improving light position in a growth chamber through the use of a genetic algorithm. In D. Plemenos, & G. Miaoulis (Eds.), *Artificial intelligence techniques for computer graphics, 159* pp. 67–82). Springer. <Go to ISI>://WOS:000262977200005.

Demotes-Mainard, S., Bertheloot, J., Boumaza, R., Huché-Thélier, L., Guéritaine, G., Guérin, V., et al. (2013). Rose bush leaf and internode expansion dynamics: Analysis and development of a model capturing interplant variability. *Frontiers in Plant Science, 4*. https://doi.org/10.3389/fpls.2013.00418

Demotes-Mainard, S., Huché-Thélier, L., Morel, P., Boumaza, R., Guérin, V., & Sakr, S. (2013). Temporary water restriction or light intensity limitation promotes branching in rose bush. *Scientia Horticulturae, 150*, 432–440. https://doi.org/10.1016/j.scienta.2012.12.005

Demotes-Mainard, S., Péron, T., Corot, A., Bertheloot, J., Le Gourrierec, J., Pelleschi-Travier, S., et al. (2016). Plant responses to red and far-red lights, applications in horticulture. *Environmental and Experimental Botany, 121*, 4–21. http://www.sciencedirect.com/science/article/pii/S0098847215000933.

Dieleman, J. A., De Visser, P. H. B., Meinen, E., Grit, J. G., & Dueck, T. A. (2019). Integrating morphological and physiological responses of tomato plants to light quality to the crop level by 3D modeling. *Frontiers in Plant Science, 10*(839). https://doi.org/10.3389/fpls.2019.00839

Escobar-Gutierrez, A. J., Combes, D., Rakocevic, M., de Berranger, C., Eprinchard-Ciesla, A., Sinoquet, H., et al. (2009). Functional relationships to estimate morphogenetically active radiation (MAR) from PAR and solar broadband irradiance measurements: The case of a sorghum crop. *Agricultural and Forest Meteorology, 149* (8), 1244–1253. https://doi.org/10.1016/j.agrformet.2009.02.011

Evers, J. B., Vos, J., Chelle, M., Andrieu, B., Fournier, C., & Struik, P. C. (2007). Simulating the effects of localized red:far-red ratio on tillering in spring wheat (Triticum aestivum) using a three-dimensional virtual plant model. *New Phytologist, 176*(2), 325–336.

Evers, J. B., Vos, J., Yin, X., Romero, P., van der Putten, P. E. L., & Struik, P. C. (2010). Simulation of wheat growth and development based on organ-level photosynthesis and assimilate allocation. *Journal of Experimental Botany, 61*(8), 2203–2216. https://doi.org/10.1093/jxb/erq025

Garbez, M., Galopin, G., Sigogne, M., Favre, P., Demotes-Mainard, S., & Symoneaux, R. (2015). Assessing the visual aspect of rotating virtual rose bushes by a labeled sorting task. *Food Quality and Preference, 40*, 287–295. Part B(0) http://www.sciencedirect.com/science/article/pii/S095032931400127X.

Henke, M., & Buck-Sorlin, G. G. (2017). Using a full spectral raytracer for calculating light microclimate in functional-structural plant modelling. *Computing and Informatics, 36*(6), 1492–1522. https://doi.org/10.4149/cai_2017_6_1492

Hitz, T., Graeff-Hönninger, S., & Munz, S. (2020). Modelling of soybean (*Glycine max* (L.) Merr.) response to blue light intensity in controlled environments. *Plants, 9*(1757). https://doi.org/10.3390/PLANTS9121757

Hitz, T., Henke, M., Graeff-Hönninger, S., & Munz, S. (2018). Simulating light spectrum within a soybean canopy in an LED growth chamber. *2018 6th international symposium on plant growth modeling, simulation, visualization and applications (PMA)*.

Hitz, T., Henke, M., Graeff-Hönninger, S., & Munz, S. (2019). Three-dimensional simulation of light spectrum and intensity within an LED growth chamber. *Computers and Electronics in Agriculture, 156*, 540–548. http://www.sciencedirect.com/science/article/pii/S0168169918308330.

Kahlen, K., & Stützel, H. (2011). Modelling photo-modulated internode elongation in growing glasshouse cucumber canopies. *New Phytologist, 190*, 697–708.

Kalaitzoglou, P., Taylor, C., Calders, K., Hogervorst, M., van Ieperen, W., Harbinson, J., et al. (2021). Unraveling the effects of blue light in an artificial solar background light on growth of tomato plants. *Environmental and Experimental Botany, 184*, Article 104377. https://doi.org/10.1016/j.envexpbot.2021.104377

Kim, J., Kang, W. H., & Son, J. E. (2020). Interpretation and evaluation of electrical lighting in plant factories with ray-tracing simulation and 3D plant modeling. *Agronomy, 10*(10), 1545. https://www.mdpi.com/2073-4395/10/10/1545.

Lee, H. J., Moon, Y. H., An, S., Sim, H., Woo, U. J., Hwang, H., et al. (2023). Determination of LEDs arrangement in a plant factory using a 3D ray-tracing simulation and evaluation on growth of cucurbitaceae seedlings. *Horticulture Environment and Biotechnology, 64*(5), 765–774. https://doi.org/10.1007/s13580-023-00523-0

Luquet, D., Dingkuhn, M., Kim, H., Tambour, L., & Clement-Vidal, A. (2006). EcoMeristem, a model of morphogenesis and competition among sinks in rice. 1. Concept, validation and sensitivity analysis. *Functional Plant Biology, 33*(4), 309–323. https://doi.org/10.1071/fp05266

Mathieu, A., Cournède, P. H., Letort, V., Barthélémy, D., & de Reffye, P. (2009). A dynamic model of plant growth with interactions between development and functional mechanisms to study plant structural plasticity related to trophic competition. *Annals of Botany, 103*(8), 1173–1186. https://doi.org/10.1093/aob/mcp054

Natale, S., Tomasella, M., Gargiulo, S., Petruzzellis, F., Tromba, G., Boccato, E., et al. (2023). Stem photosynthesis contributes to non-structural carbohydrate pool and modulates xylem vulnerability to embolism in *Fraxinus ornus* L. *Environmental and Experimental Botany, 210*, Article 105315. https://doi.org/10.1016/j.envexpbot.2023.105315. Article 105315.

Noda, H. M., Muraoka, H., & Nasahara, K. N. (2021). Phenology of leaf optical properties and their relationship to mesophyll development in cool-temperate deciduous broad-leaf trees. *Agricultural and Forest Meteorology, 297*, Article 108236. https://doi.org/10.1016/j.agrformet.2020.108236

Pharr, M., Wenzel, J., & Humphreys, G. (2016). *Physically based rendering. From theory to implementation* (3rd ed. ed.). Morgan Kaufmann. https://doi.org/10.1016/C2013-0-15557-2

Pradal, C., Boudon, F., Nouguier, C., Chopard, J., & Godin, C. (2009). PlantGL: A Python-based geometric library for 3D plant modelling at different scales. *Graphical Models, 71*(1), 1–21. https://doi.org/10.1016/j.gmod.2008.10.001

Pradal, C., Dufour-Kowalski, S., Boudon, F., Fournier, C., & Godin, C. (2008). OpenAlea: A visual programming and component-based software platform for plant modelling. *Functional Plant Biology, 35*(10), 751–760. https://doi.org/10.1071/FP08084

Pradal, C., Fournier, C., Valduriez, P., & Cohen-Boulakia, S. (2015). *OpenAlea: Scientific workflows combining data analysis and simulation proceedings of the 27th International conference on scientific and statistical database management*. California: La Jolla. https://doi.org/10.1145/2791347.2791365

Roman, H., Girault, T., Barbier, F., Péron, T., Brouard, N., Pencik, A., et al. (2016). Cytokinins are initial targets of light in the control of bud outgrowth. *Plant Physiology, 172*, 489–509.

Saito, K., Ishigami, Y., & Goto, E. (2020). Evaluation of the light environment of a plant factory with artificial light by using an optical simulation. *Agronomy, 10*(11), 1663. https://www.mdpi.com/2073-4395/10/11/1663.

Sarlikioti, V., de Visser, P. D., & Marcelis, L. (2011). Exploring the spatial distribution of light interception and photosynthesis of canopies by means of a functional-structural plant model. *Annals of Botany, 107*(5), 875–883. https://doi.org/10.1093/AOB/MCR006

Sarlikioti, V., de Visser, P. H. B., Buck-Sorlin, G. H., & Marcelis, L. F. M. (2011). How plant architecture affects light absorption and photosynthesis in tomato: Towards an ideotype for plant architecture using a functional-structural plant model. *Annals of Botany, 108*(6), 1065–1073. https://doi.org/10.1093/aob/mcr221

Schneider, A., Godin, C., Boudon, F., Demotes-Mainard, S., Sakr, S., & Bertheloot, J. (2019). Light regulation of axillary bud outgrowth along plant axes: An overview of the roles of sugars and hormones. *Frontiers in Plant Science, 10*(1296). https://doi.org/10.3389/fpls.2019.01296

Wang, M., Pérez-Garcia, M. D., Davière, J. M., Barbier, F., Ogé, L., Gentilhomme, J., et al. (2021). Outgrowth of the axillary bud in rose is controlled by sugar metabolism and signalling. *Journal of Experimental Botany, 72*(8), 3044–3060. https://doi.org/10.1093/jxb/erab046

Wiechers, D., Kahlen, K., & Stützel, H. (2011). Evaluation of a radiosity based light model for greenhouse cucumber canopies. *Agricultural and Forest Meteorology, 151*(7), 906–915. https://doi.org/10.1016/j.agrformet.2011.02.016

Wubs, A. M., Heuvelink, E., Marcelis, L. F. M., Buck-Sorlin, G. H., & Vos, J. (2014). Axillary budbreak in a cut rose crop as influenced by light intensity and red:far-red ratio at bud level. *Journal of the American Society for Horticultural Science, 139*(2), 131–138. <Go to ISI>://WOS:000334148300005.

Yavari, N., Tripathi, R., Wu, B. S., MacPherson, S., Singh, J., & Lefsrud, M. (2021). The effect of light quality on plant physiology, photosynthetic, and stress response in *Arabidopsis thaliana* leaves. *PLoS One, 16*(3), Article e0247380. https://doi.org/10.1371/journal.pone.0247380

Zambrano-Bigiarini, M. (2024). hydroGOF: Goodness-of-fit functions for comparison of simulated and observed hydrological time series. https://cran.r-project.org/package=hydroGOF.

Zhang, N., van Westreenen, A., Anten, N. P. R., Evers, J. B., & Marcelis, L. F. M. (2020). Disentangling the effects of photosynthetically active radiation and red to far-red ratio on plant photosynthesis under canopy shading: A simulation study using a functional-structural plant model. *Annals of Botany, 126*(4), 635–646. https://doi.org/10.1093/aob/mcz197

Zhang, Y., Henke, M., Li, Y., Yue, X., Xu, D., Liu, X., et al. (2020). High resolution 3D simulation of light climate and thermal performance of a solar greenhouse model under tomato canopy structure. *Renewable Energy, 160*, 730–745. https://doi.org/10.1016/j.renene.2020.06.144